TOPICAL REVIEW — A 40th Anniversary Celebration: Physics Research and Innovation at Ningbo University

Review of three-dimensional graphene photodetectors: advances in mechanisms, architectures, and applications

Shubo Li(李舒博), Kuan Qian(钱宽), Fanghao Zhu(朱昉昊), Hui Ma(马慧), Genqiang Cao(曹根强), Shanshui Lian(连山水), Jinqiu Zhang(张金秋), Wenwu Xu(许文武)[†], Xu Wang(王旭)[‡], and Gang Wang(王刚)[§]

School of Physical Science and Technology, Ningbo University, Ningbo 315211, *China*

(Received 31 May 2026; revised manuscript received 31 July 2026; accepted manuscript online 17 August 2026)

As a three-dimensional (3D) extension of two-dimensional (2D) graphene, it retains impressive properties such as high carrier mobility, electrical conductivity, and interfacial compatibility. Its unique porous network enhances optical field distribution and carrier dynamics, offering a higher specific surface area and greater active edge density than traditional semiconductor materials. This makes it an excellent candidate for advanced photodetection. Features such as nano-resonant cavities enhance light-absorption efficiency through photon confinement and scattering. Its zero-bandgap semimetallic nature enables devices to achieve a wide spectral response from the ultraviolet to the terahertz range. With a work function of 4.5 eV to 4.8 eV, 3D-graphene forms high-quality Schottky heterojunctions with semiconductors including silicon (Si), germanium (Ge), gallium arsenide (GaAs), and indium phosphide (InP), enhancing photogenerated charge carrier separation. Thus, 3D-graphene photodetectors show great potential for broadband response, high sensitivity, and compatibility with complementary metal-oxide-semiconductor (CMOS) technology. This review summarizes recent advances in 3D-graphene photodetectors, focusing on structural design and performance relationships while exploring applications in optoelectronic logic, polarization imaging, and information encryption.

Keywords: 3D-graphene, broadband response, Schottky heterojunction, multifunctional applications

PACS: 81.05.ue, 85.60.Gz, 73.30.+y, 73.40.Lq

DOI: 10.1088/1674-1056/ae9a5e **CSTR:** 32038.14.CPB.ae9a5e

1. Introduction

Photodetection technology serves as a vital interface between optical and electronic information by converting light signals across various wavelengths into electrical signals that can be processed. This capability facilitates information acquisition and energy conversion across the spectrum from ultraviolet to terahertz.[1–5] Its significance spans multiple domains, including environmental monitoring, satellite remote sensing, biomedicine, national defense and security, high-speed optical communication, and artificial intelligence visual perception.[6–11] With rapid advances in intelligent sensing, integrated optoelectronics, and on-chip information processing technologies, there is a continuous evolution of novel photodetectors characterized by broadband spectral response, high sensitivity, rapid response times, low power consumption, and seamless on-chip integration.[12–16] The core driver of these advancements lies in the innovation of material systems. For these rapidly evolving devices, standardized characterization of key figures of merit is essential to enable objective comparisons across different materials and device architectures and to evaluate the compatibility of laboratory prototypes with industrial technologies.[17] The transition from traditional silicon (Si) based semiconductors and III–V compound semiconductors to next-generation low-dimensional nanomaterials has broadened the operational parameters and application potential of photodetectors.[18,19]

The advent of two-dimensional (2D) graphene in 2004 ushered in new opportunities for the advancement of innovative broadband photodetection technologies.[20] As a semimetal with a zero bandgap, graphene exhibits ultrahigh carrier mobility, low intrinsic noise, and compatibility with Si-based processes, overcoming the spectral response limitations associated with conventional semiconductors. This allows for a broadband photoresponse spanning from ultraviolet to mid-infrared wavelengths.[21–23] However, the integration of 2D graphene in photodetectors is still hampered by its intrinsic structural limitations. The atomically thin nature of graphene results in an optical absorption capacity of approximately 2.3%,[24] which falls short of the requirements for efficient photoelectric conversion. The zero bandgap also contributes to diminished carrier lifetime in devices, which constrains sensitivity enhancements.[25,26] Despite advancements in device performance through techniques such as sur-

[†]Corresponding author. E-mail: xuwenwu@nbu.edu.cn
[‡]Corresponding author. E-mail: wangxu1@nbu.edu.cn
[§]Corresponding author. E-mail: gangwang@nbu.edu.cn

© 2026 Chinese Physical Society and IOP Publishing Ltd. All rights, including for text and data mining, AI training, and similar technologies, are reserved.

CPB Online In Press

face modification, heterostructure fabrication, band engineering, and plasmonic enhancement, achieving a synergistic balance between light absorption enhancement and the short carrier lifetime in 2D planar architectures remains a significant challenge.[27–33] Consequently, enhancing the light field modulation capability while preserving graphene's excellent electrical transport properties is a crucial goal for the development of graphene-based photodetectors.

The emergence of three-dimensional (3D) graphene offers a novel structural paradigm to address these challenges. 3D-graphene, also referred to as vertical graphene (VG), graphene nanowalls (GNWs), or carbon nanowalls (CNWs),[34] is characterized by its 3D porous network structure, resulting from the vertical growth and internal interconnectivity of 2D graphene sheets.[35] High-quality 3D-graphene is synthesized through *in-situ* growth on semiconductor substrates using plasma-enhanced chemical vapor deposition (PECVD), forming a porous network of interconnected vertically oriented graphene nanosheets.[36] This 3D architecture not only retains the high electrical conductivity and carrier mobility of 2D-graphene, but also offers distinct advantages arising from its unique spatial configuration.[37–41] Specifically: (i) The naturally occurring nano-resonant cavities within the interconnected porous framework promote light–matter interactions via multiple scattering, photon confinement, and localized electric field enhancement;[42,43] (ii) The abundant edge states and ultra-high specific surface area foster numerous active sites for the incorporation of quantum dots (QDs), metal nanoparticles (NPs), and other 2D materials;[44,45] (iii) The *in-situ* growth methodology mitigates defects and contamination typically associated with conventional transfer techniques, ensuring high-quality interfacial contact between graphene and the semiconductor, which reduces interface-related carrier recombination losses;[46] and (iv) the work function of 3D-graphene, ranging from 4.5 eV to 4.8 eV, allows the formation of high-quality Schottky heterojunctions with various semiconductors, including Si, germanium (Ge), gallium arsenide (GaAs), and indium phosphide (InP), thereby generating efficient built-in electric fields that facilitate the separation and transport of photogenerated carriers.[19,47] These combined advantages position 3D-graphene as a promising candidate material for the development of broadband, high-sensitivity, self-powered, and CMOS-compatible photodetectors.

In recent years, there has been significant progress in the development of 3D-graphene-based photodetectors,[48–51] driven by various strategies such as the construction of semiconductor heterostructures, interface engineering, doping modulation, QD integration, and micro-nano optical field modulation. These approaches have led to the optimization of key parameters including light absorption, interfacial charge transfer, and carrier transport, enabling broadband photodetection across both the ultraviolet and near-infrared spectra. The distinct spatial architecture of 3D-graphene is facilitating advancements in optoelectronic applications, including polarization detection, optoelectronic logic, visual image sensing, and information encryption.[52–56] However, a systematic understanding of the intrinsic relationships between diverse structural designs and the corresponding enhancement mechanisms is still lacking. Notably, a cohesive theoretical framework addressing how 3D geometrical configurations synergistically influence optical field distribution, interfacial electronic structures, and carrier dynamics remains to be formulated.

Previous studies have established a solid foundation for the development of 3D-graphene. Li *et al*., provided an overview of fabrication techniques and potential applications for 3D-graphene micro/nano architectures, highlighting the effectiveness of 3D assembly in enhancing surface area accessibility and improving mass and charge transport.[57] Fang *et al*. examined synthesis routes, surface modification strategies, structural characteristics, and physicochemical properties of 3D-graphene macrostructures, offering insights for controlled fabrication and functionalization efforts.[58] Peurifoy *et al*. demonstrated that molecularly engineered 3D-graphene nanostructures improve optical absorption and minimize interfacial contact resistance in optoelectronic devices, illustrating how 3D topology influences light–matter interaction and charge dynamics.[59] While these studies serve as a foundation for structural design, functionalization, and optoelectronic property evaluation of 3D-graphene, they do not primarily address vertically grown 3D-graphene photodetectors. More recently, Wang *et al*. conducted a comprehensive review of growth techniques, physical characteristics, device classifications, operational mechanisms, performance metrics, and the key challenges associated with 3D-graphene photodetectors.[60] However, there remains a lack of a unified framework that correlates controllable structural and interfacial parameters with optical-field modulation, carrier dynamics, and quantifiable photodetection performance. Furthermore, despite reports of optoelectronic logic and imaging demonstrations, a systematic analysis of 3D-graphene devices for integrated logic operations, information encryption, imaging, and flexible sensing in relation to structural and interfacial design principles is still needed. This review seeks to address these gaps by focusing on the structure–performance relationships of 3D-graphene photodetectors, integrating recent advancements in the field, and comparing their multifunctional applications. In doing so, we aim to elucidate how structural and interfacial engineering can facilitate the transition from traditional photodetection to multifunctional optoelectronic sensing and information processing.

Building on these previous studies, this review aims to address these gaps by providing a comprehensive analysis

CPB Online In-Press

of the fundamental physical characteristics of 3D-graphene. We systematically explore its growth mechanisms, structural attributes, optical absorption behaviors, electrical transport dynamics, interface engineering strategies, and principles of morphology control. A key focus is placed on delineating the structure–performance relationships that elucidate how optical field enhancement, interfacial charge transfer, and carrier transport are modulated by the unique 3D architecture. Furthermore, we will scrutinize the operational mechanisms and performance optimization strategies of various types of 3D-graphene-based photodetectors. Through comparative case studies, we will summarize critical performance metrics such as responsivity, specific detectivity, response speed, and spectral range. A thorough discussion will follow, assessing the strengths and limitations of different optimization techniques in areas such as light absorption enhancement, dark current suppression, interface composite tuning, and broadband response expansion. This is intended to provide theoretical insights and technical guidance for the design and application of high-performance 3D-graphene optoelectronic devices, supported by relevant illustrations (Fig. 1).

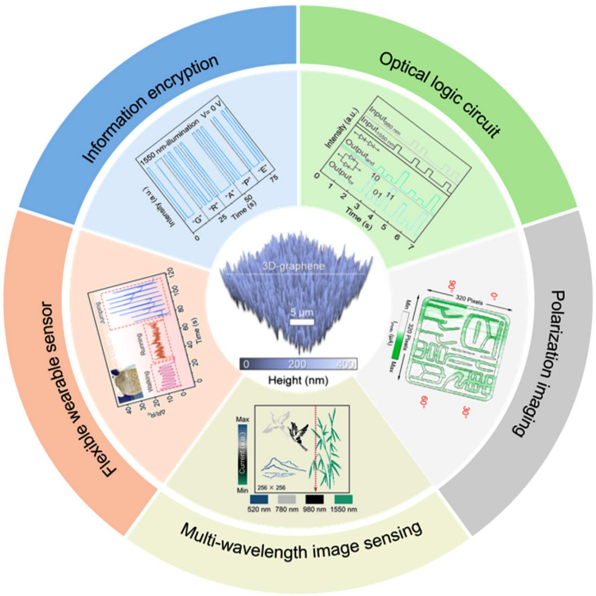


Fig. 1. Applications of 3D-graphene photodetectors.

2. Physical properties of 3D-graphene

3D-graphene is synthesized through *in-situ* growth on semiconductor substrates using PECVD, resulting in a 3D porous network comprised of interconnected vertically aligned graphene nanosheets.[35,36] This architecture distinguishes 3D-graphene from its 2D counterpart by maintaining its intrinsic properties of high electrical conductivity and superior carrier mobility, while simultaneously enhancing capabilities in optical field modulation, interfacial interaction, and carrier transport dynamics.[61,62] This section provides a comprehensive analysis of the intrinsic relationships between the structural attributes, physical properties, and optoelectronic functionalities of 3D-graphene, focusing on structural characteristics, electrical transport mechanisms, interface modulation strategies, and morphology engineering techniques.

2.1. Basic structure of 3D-graphene

Atomic force microscopy (AFM) characterization reveals that the 3D-graphene is composed of vertically oriented graphene nanosheets, creating a highly interconnected porous network (Figs. 2(a) and 2(b)). This architecture features an impressive porosity of up to 83% and an exceptionally high specific surface area.[63,64] Such attributes enable a significant number of adsorption sites for QDs, metal NPs, and 2D materials.[44,45] Consequently, this structure is extensively utilized in the fabrication of composite optoelectronic architectures.

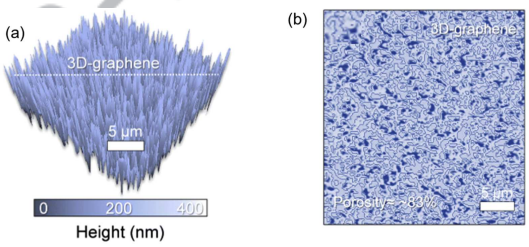


Fig. 2. (a) AFM image of the 3D-graphene. (b) Porosity of the 3D-graphene.[63]

Semiconductor QDs such as lead sulfide (PbS), molybdenum disulfide (MoS_2), tungsten disulfide (WS_2), and carbon nitride (C_3N) exhibit size-tunable band gaps.[65–68] enabling the extension of detection wavelengths for Si-based devices into the near-infrared and short-wave infrared regions. However, these materials are susceptible to interfacial recombination of photogenerated carriers.[69] The porous structure of 3D-graphene facilitates a uniform distribution of QDs, constructing efficient charge transport pathways. In Fig. 3(a), a cross-sectional scanning electron microscope (SEM) image shows the PbS QDs/3D-graphene/Si heterojunction. PbS QDs are well-dispersed throughout the 3D-graphene pores.[70] Finite-difference time-domain (FDTD) simulation results[71] (Figs. 3(b) and 3(c)) reveal a significant enhancement in localized electric field and power dissipation density upon the incorporation of QDs, showing a synergistic effect in light absorption between the 3D-graphene nano-resonant cavities and the QDs. Moreover, metal NPs can also contribute to synergistic enhancement when integrated with 3D-graphene.[72] As illustrated in Figs. 3(d)–3(f), the deposition of Ag-NPs creates pronounced electric field enhancement regions by coupling localized surface plasmon resonance (LSPR) with nano-resonant cavities in 3D-graphene, thereby enhancing light absorption and optical field localization.

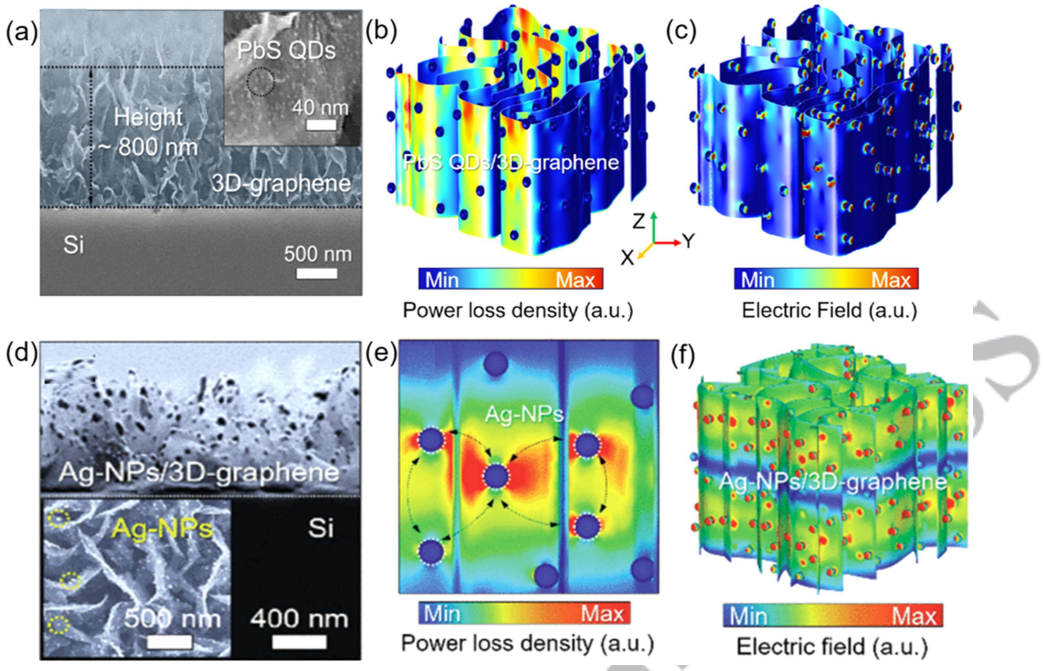


Fig. 3. (a) Cross-section SEM image of PbS QDs/3D-graphene/Si, with surface morphology inset.[70] (b) Power loss density distribution and (c) electric field distribution in the PbS QDs/3D-graphene structure.[71] (d) Cross-section SEM of Ag-NPs/3D-graphene/Si, with magnified inset. (e) Power loss density distribution and (f) electric field distribution of the Ag-NPs/3D-graphene/Si structure.[72]

2.2. Electrical properties of 3D-graphene

The interfacial charge transfer dynamics of the Schottky heterojunction formed at the interface between 3D-graphene and semiconductor substrates are analyzed at the nanoscale using scanning Kelvin probe microscopy (SKPM) and conductive AFM (C-AFM).[73] As shown in Fig. 4(a), SKPM measures the contact potential difference (V_{CPD}) between the probe and the sample to map the surface potential distribution. Figures 4(b)–4(e) illustrate that the surface potential of the 3D-graphene/Si-on-insulator (SOI) heterojunction increases under illumination, with V_{CPD} rising from 150 mV in the dark to 210 mV. This enhancement suggests that light exposure facilitates interfacial charge redistribution and carrier transfer. C-AFM results provide insight into the localized conductive properties of the 3D-graphene structure. As depicted in Fig. 4(g), current transport primarily occurs along the vertically aligned graphene sheets, while the regions between the sheets exhibit diminished conductivity. This observation confirms that the vertical architecture of the graphene fosters effective carrier transport pathways. Additionally, the *I*–*V* characteristics illustrated in Fig. 4(f) display rectifying behavior, further substantiating the formation of a Schottky heterojunction at the 3D-graphene/SOI interface.

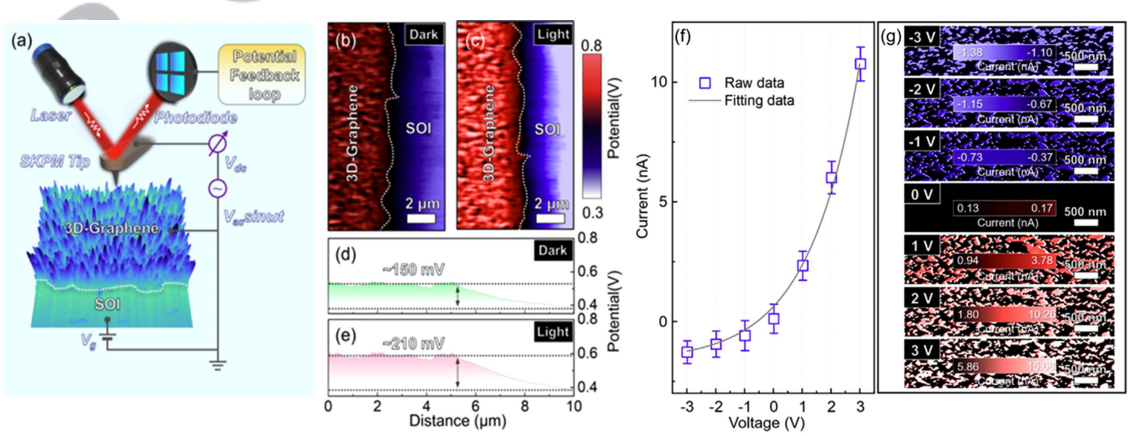


Fig. 4. (a) Diagram of SKPM used for 3D-graphene/SOI heterojunction characterization. (b) Surface potential in the dark. (c) Surface potential under light. (d) Surface potential variation perpendicular to the interface in the dark. (e) Variation under light. (f) *I*–*V* curve for the 3D-graphene/SOI surface from current maps in (g). (g) C-AFM current maps of the surface at different bias voltages.[73]

2.3. Controllable interface of 3D-graphene

In the Schottky heterojunction formed by the direct interface between 3D-graphene and semiconductors, two significant challenges arise at the contact interface. The first issue is the inadequate passivation at the 3D-graphene/semiconductor boundary, which results in a high surface density of states (DOS) and consequently leads to considerable leakage

currents.[74] The second challenge stems from the formation of an amorphous carbon (AC) transition layer, typically 3–5 nm thick, during the growth of 3D-graphene. This disordered AC layer introduces numerous defects and scattering centers, diminishing the efficacy of charge transport at the interface. Therefore, engineering the interface is crucial for optimizing the performance of 3D-graphene-based photodetectors.[24,75]

Incorporating an Al_2O_3 high-κ dielectric layer between 3D-graphene and Si forms a metal–insulator–semiconductor (MIS) tunneling structure,[76] enhancing interfacial defect passivation and selective carrier transport. The SEM image in Fig. 5(a) shows the layered 3D-graphene/Al_2O_3/Si architecture. SKPM in Fig. 5(b) indicates improved interfacial carrier separation under illumination. FDTD simulations reveal that the inclusion of the high-κ layer enhances optical field localization and light absorption efficiency (Figs. 5(c) and 5(d)). In addition to high-κ dielectrics, the insertion of a 2D-graphene interlayer serves as another effective strategy for interface optimization. Positioning 2D-graphene between the 3D-graphene and Ge allows for the replacement of the AC transition layer and improves the interfacial electronic structure. Density functional theory (DFT) calculation results[77] (Figs. 5(e) and 5(f)) show that the 2D-graphene interlayer boosts interfacial electronic DOS and coupling, enhancing light absorption and carrier transport.

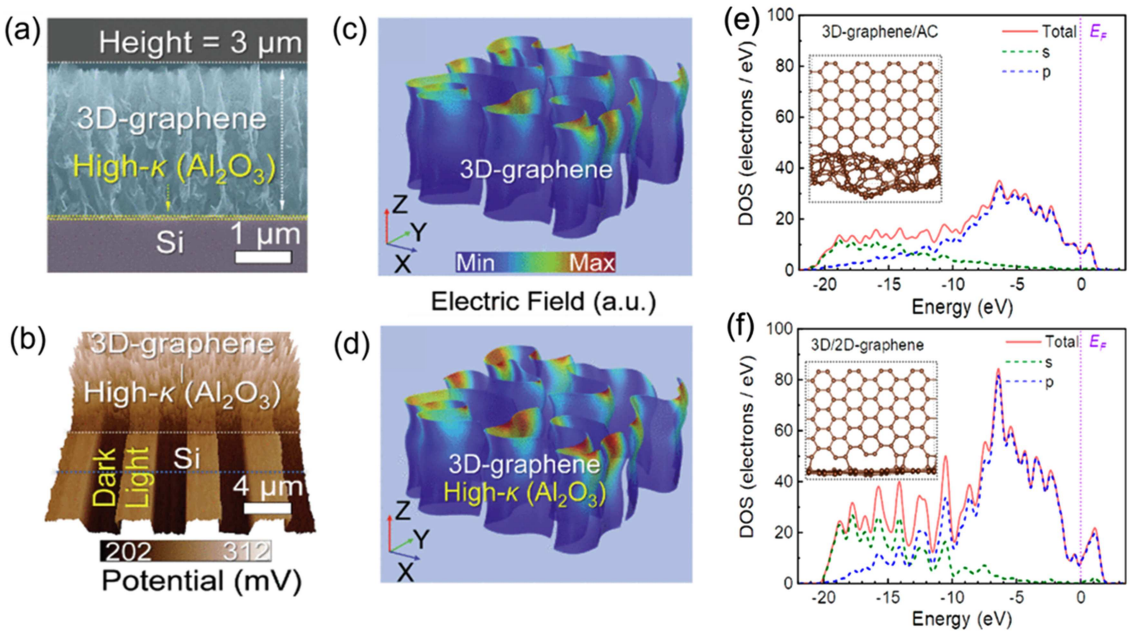


Fig. 5. (a) Cross-sectional SEM image of the thin high-κ photodetector (THPD). (b) Surface potential of the THPD. 3D electric field distributions in (c) HPD and (d) THPD.[76] Surface electronic DOS of (e) 3D-graphene/AC and (f) 3D/2D-graphene systems based on DFT calculations, with 0 eV marking the Fermi levels of the systems.[77]

2.4. Shape regulation of 3D-graphene

The spatial geometric structure of 3D-graphene is intricately linked to its optical field distribution, interfacial charge transfer dynamics, and carrier transport characteristics.[78–81] By manipulating parameters such as nanosheet curvature, porosity, edge density, and growth direction, one can tailor the local electric field distribution, band structure, and light absorption capabilities. Nitrogen (N) doping plays a pivotal role in modulating the growth kinetics, resulting in a hydrangea-like hierarchical architecture. DFT calculation results (Figs. 6(a)–6(d)) indicate[54] that N-doping elevates the work function of graphene, thereby enhancing its interfacial charge transfer efficiency. Furthermore, the curvature-induced localized plasmon resonance (CLPR) arising from the morphology and nanogaps produces intense localized electric field hotspots between the petals (Figs. 6(e) and 6(f)).[82] The seaweed-like graphene synthesized from a low-pressure liquid ethanol carbon source develops a porous, curled network structure (Fig. 6(g)).[83] FDTD simulations (Fig. 6(h)) indicate the formation of multiple nano-resonant cavities within these curled sheets. The incident light experiences extensive scattering and reflection within these cavities, which extends the optical path length and boosts light absorption, achieving rates up to 89%. Additionally, the bio-inspired cat's eye structure enhances the light field modulation capability of 3D-graphene.[84] In the 3D-graphene/anodic aluminum oxide (Al-AAO) configuration, characterized by an aluminized inner layer, as shown in Figs. 6(i) and 6(j), the reflective cavities on the inner walls of Al-AAO and the 3D-graphene resonant cavities form synergistic coupling, enabling secondary reflection and repeated absorption of unabsorbed light. FDTD simulation results (Figs. 6(k) and 6(l)) further reveal substantial enhancements in local electric fields and power dissipation regions within the composite structure, improving light utilization efficiency.

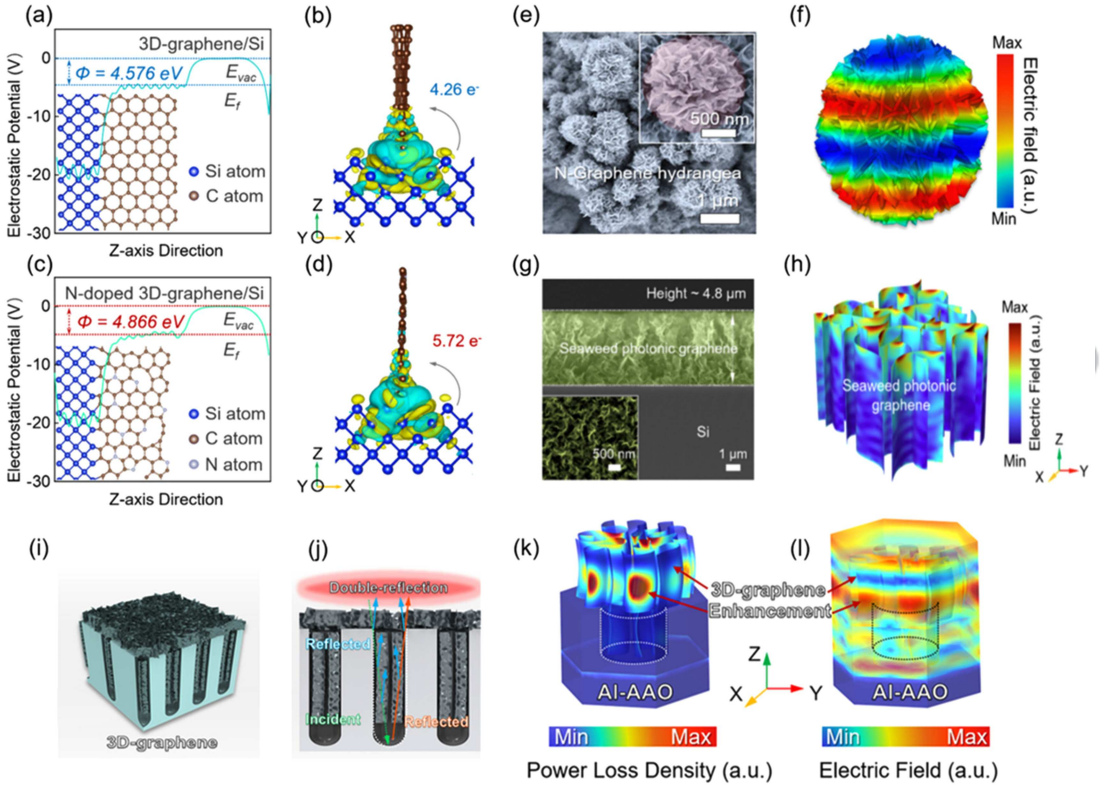


Fig. 6. (a) Electrostatic potential of the 3D-graphene/Si along the *Z*-direction. (b) Side view of charge density difference. (c) Electrostatic potential of N-doped 3D-graphene/Si along the *Z*-direction. (d) Charge density difference for N-doped 3D-graphene/Si; yellow indicates electron accumulation, cyan indicates depletion.[54] (e) SEM of N-graphene hydrangea/Si surface. (f) Normalized electric field distribution of N-graphene hydrangea/Si.[82] (g) Cross-sectional SEM of Seaweed photonic graphene/Si. (h) Electric field distribution at the junction.[83] (i) 3D-graphene/Al-AAO biomimetic structure. (j) Schematic of dual light reflection paths. (k) Normalized power loss density and (l) normalized electric field distribution of 3D-graphene/Al-AAO based on FDTD simulations.[84]

3. 3D-graphene-based photodetectors

3D-graphene exhibits the properties of a zero-bandgap semimetal,[85] facilitating the formation of Schottky heterojunctions with various semiconductors, including Si, Ge, GaAs, and InP, through metal–semiconductor contacts without the necessity for precise lattice alignment,[19,22] thereby exhibiting excellent process compatibility. In contrast to traditional semiconductor photodetectors, 3D-graphene functions as a carrier transport channel, leveraging the built-in electric field of the Schottky junction to efficiently separate photogenerated charge carriers and modulate channel conductivity, thereby generating a notable photoresponse.[86] However, the direct-contact configuration of 3D-graphene with semiconductors is hindered by several challenges, including elevated dark currents, inadequate near-infrared absorption, pronounced interfacial recombination, and restricted mechanical flexibility. To address these issues, researchers are exploring various strategies such as heterojunction optimization, doping strategies, interface engineering, quantum dot integration, optical field enhancement, and the adoption of flexible substrates (Fig. 7). Specifically, efforts have focused on: (i) broadening the response spectral range through the integration of multiple semiconductor materials; (ii) tuning the Fermi level and barrier height via nitrogen doping; (iii) improving interfacial transport characteristics by incorporating high-κ tunneling layers; (iv) extending the spectral response into the short-wave infrared region through QDs incorporation; (v) enhancing optical field coupling using plasmonics, resonant cavity designs, and patterned structures; and (vi) enabling strain modulation and wearable applications with flexible supports. Advancements along these lines have led to the evolution of 3D-graphene photodetectors, transitioning from basic broadband photodetection to sophisticated applications in logic operations, image sensing, and flexible optoelectronic integration.

3.1. 3D-graphene/semiconductor heterojunction photodetectors

3.1.1. Working principle of 3D-graphene/semiconductor heterojunction

3D-graphene demonstrates weakly p-type conductivity in ambient conditions, with a work function ranging from approximately 4.5 eV to 4.8 eV. This creates a favorable work function difference when compared to semiconductors like SOI (4.1 eV), Si (4.3 eV), and Ge (3.62 eV), facilitating the spontaneous formation of Schottky heterojunctions upon physical contact.[87–89] The photoelectric conversion process can be delineated into three primary stages: charge transfer, the establishment of a built-in electric field, and the separation and transport of photogenerated carriers. In the 3D-graphene/SOI heterojunction case study,[73] as shown in

Fig. 8(a), the Fermi levels of the materials differ before contact, with SOI having a higher level. This causes electrons to migrate from SOI to 3D-graphene until thermal equilibrium is reached, creating a built-in electric field at their interface directed from SOI to 3D-graphene. As shown in Fig. 8(b), after equilibrium, the band bends upward on the SOI side, while the change on the 3D-graphene side is relatively small. When the incident photon energy exceeds the band gap of the semiconductor, the semiconductor absorbs photons and generates electron-hole pairs. Under the built-in electric field, holes drift toward 3D-graphene and are collected by the top electrode, while electrons migrate into the interior of the semiconductor and are collected by the bottom electrode, thus forming a directional photocurrent, as illustrated in Fig. 8(c). This mechanism enables 3D-graphene/semiconductor heterojunctions to achieve efficient broadband photodetection, and the response can be extended from the visible to the near-infrared region by selecting different semiconductors.

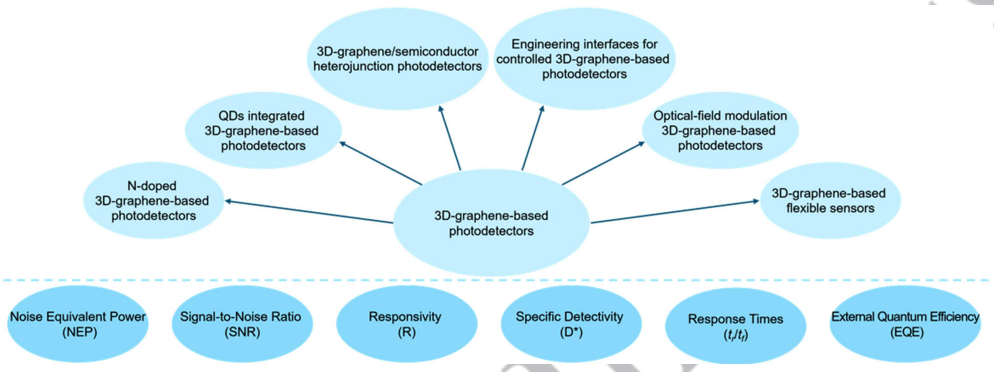


Fig. 7. Schematic overview of 3D-graphene photodetector configurations and key performance metrics.

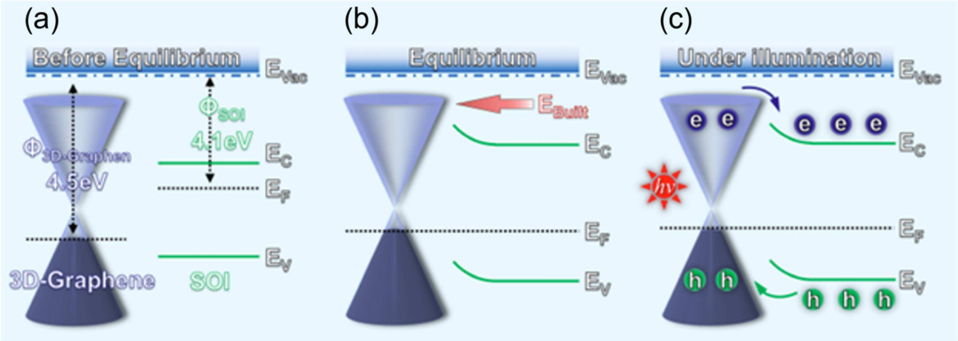


Fig. 8. Energy band diagrams of 3D-graphene/SOI: (a) before equilibrium, (b) at equilibrium, and (c) in light.[73]

3.1.2. 3D-graphene/Si Schottky heterojunction photodetectors

The optical characterization of the heterojunction comprising vertically aligned graphene nanowall arrays (VAGNAs), also known as 3D-graphene, integrated with Si (VAGNAs/Si), is presented in Fig. 9(a).[90] The device exhibits a remarkable photoresponse across a broad spectral range of 380 nm to 1550 nm, as depicted in Fig. 9(b), achieving a responsivity of 66 A/W and a specific detectivity of 7.3×10^{10} Jones, and rapid response times of 178 μs (rise time) and 186 μs (fall time) (Fig. 9(c)). The device maintains significant temperature stability, operating between 218 K and 388 K (Fig. 9(d)), while offering 180 × 180 pixels multi-wavelength imaging capabilities (Fig. 9(e)), indicating its potential for broadband imaging applications. Additionally, the 6-inch wafer-scale VAGNAs exhibit excellent spatial uniformity and durability, establishing a solid groundwork for large-scale integration.

Lian *et al.*[83] employed ethanol-PECVD for *in-situ* growth to address the challenges associated with graphene transfer. This method enables the formation of a defect-free heterointerface, leading to the development of a Seaweed photonic graphene/Si heterojunction photodetector. The bioinspired porous branched architecture improves interfacial light absorption and carrier mobility, resulting in a stable operational response across a spectral range of 440–1550 nm (Figs. 10(a) and 10(b)). At 1550 nm, it achieves a responsivity of 82 A/W, a specific detectivity of 1.1×10^{11} Jones, and rapid response times of 130 μs for rise time and 154 μs for fall time (Fig. 10(c)). As shown in Figs. 10(d)–10(f), under self-powered conditions, the photocurrent polar plot stimulated by a 1550 nm polarized laser reveals a strong polarization dependence, with a polarization ratio of 1.31, indicating that the device is highly sensitive to the incident polarization direction, and 320 × 320 pixel polarization imaging has been demonstrated.

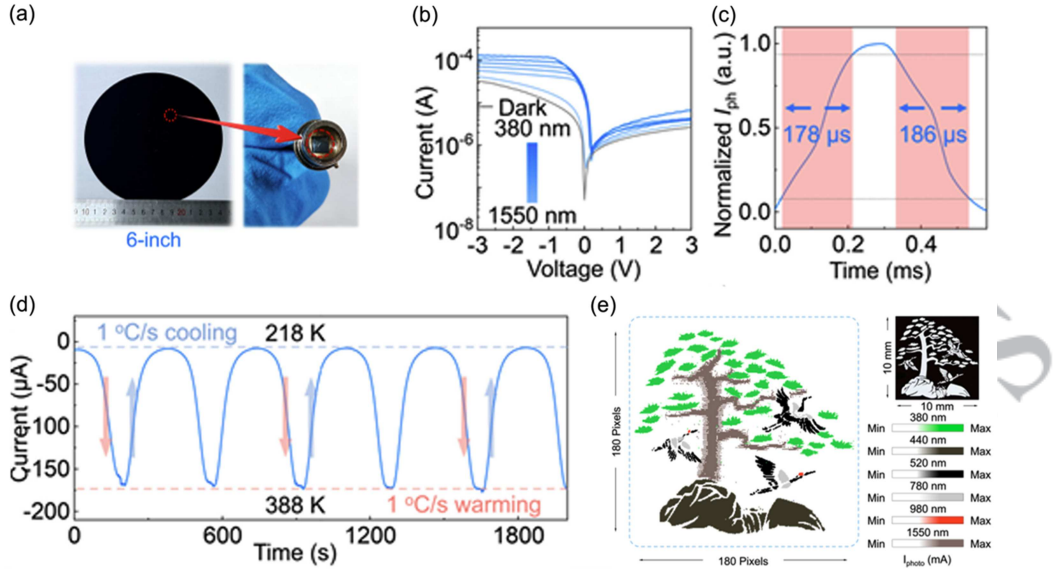


Fig. 9. (a) Optical images of VAGNAs/Si heterojunction and packaged device. (b) *I*–*V* curves. (c) t_r/t_f curves. (d) Photocurrent (218–388–218 K cycling). (e) High-resolution imaging with 380–1550 nm illumination and photomask patterns.[90]

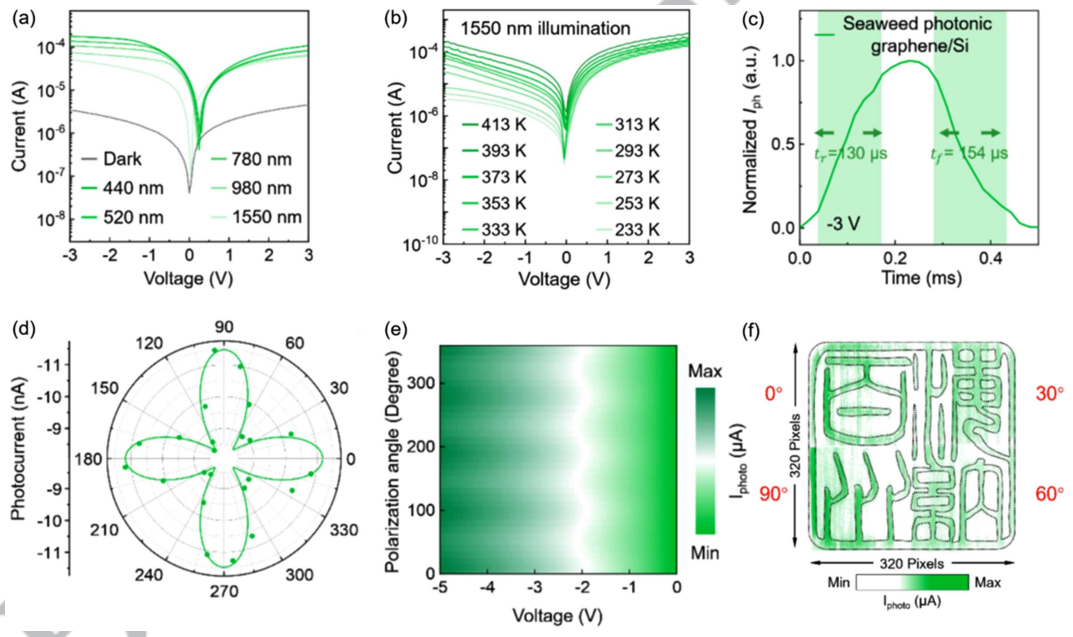


Fig. 10. (a) Broadband photoresponse curves of the Seaweed photonic graphene/Si heterojunction photodetector, spanning 440 nm to 1550 nm at 0.4 W/cm^2. (b) *I*–*V* characteristics at temperatures from 233 K to 413 K under 1550 nm light. (c) Rise and fall times of the photodetector. (d) Spatial photocurrent distribution in self-powered mode with a 1550 nm laser. (e) Thermographs of photocurrent versus polarization angle at different bias voltages. (f) High-resolution images of the device under a 1550 nm laser at varying polarization angles.[83]

3.1.3. 3D-graphene/III–V semiconductor Schottky heterojunction photodetectors

GaAs exhibits excellent electron mobility, but its intrinsic absorption cutoff wavelength is approximately 874 nm.[89,91] To broaden its near-infrared response, Wu *et al.*[92] developed a 3D-graphene/GaAs heterojunction. This device demonstrates a stable photoresponse in the 440–980 nm range (Fig. 11(a)), achieving a responsivity of 3.1 A/W, a specific detectivity of 1×10^{10} Jones, and response times of 302/295 μs (Fig. 11(b)). Under self-powered conditions at 0 V, the device performs dual-band light-controlled "AND" and "OR" gate logic operations (Figs. 11(c)–11(d)), and facilitates 310×330 pixel imaging, demonstrating its potential for integration into optoelectronic logic systems (Figs. 11(e)–11(f)).

Compared with GaAs and InP, it exhibits superior electron mobility, which enhances its application prospects in optical communication. However, the intrinsic band gap of InP, at 1.34 eV, restricts its operational range in the near-infrared spectrum.[93–95] Zhang *et al.*[55] reported the fabrication of a 3D-graphene/InP heterojunction utilizing a PECVD-assisted *in-situ* growth technique. This device demonstrates impressive broadband photodetection capabilities spanning 380–1550 nm (Fig. 12(a)), achieving a responsivity of 12.2 A/W and a specific detectivity of 2.1×10^{10} Jones. The device exhibits a noise

current of approximately 6×10^{-9} A/Hz$^{1/2}$ (Fig. 12(b)), with a cutoff frequency of 400 Hz (Fig. 12(c)), and response times of 510/390 μs (Fig. 12(d)). Notably, the device maintains stable performance under zero-bias conditions (Fig. 12(e)). Additionally, it successfully implements an American Standard Code for Information Interchange (ASCII)-encoded optical communication function (Fig. 12(f)), verifying its potential for applications in near-infrared communication systems.

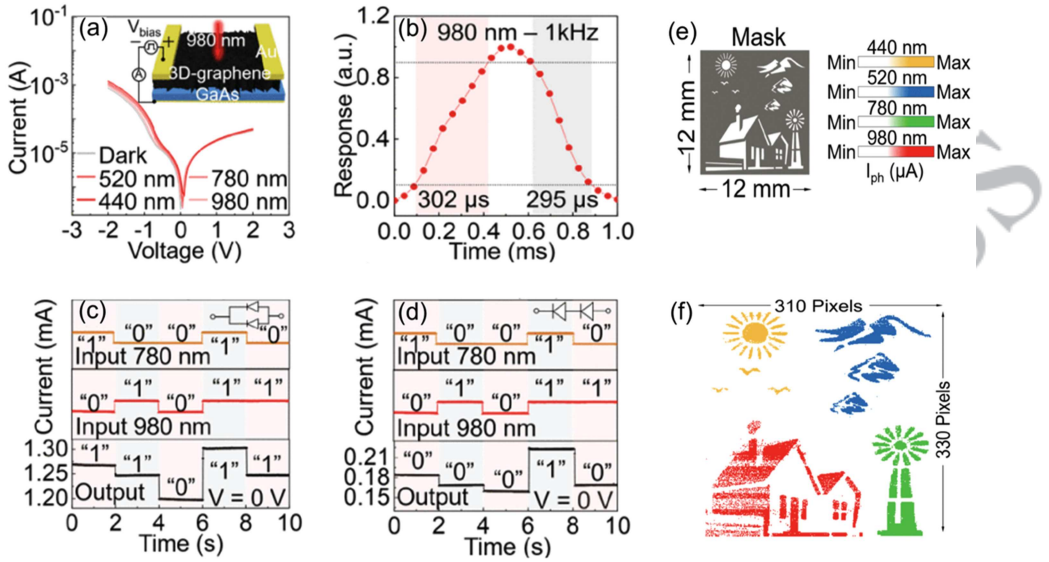


Fig. 11. (a) Rectification characteristics at wavelengths 440 nm, 520 nm, 780 nm, and 980 nm with equal power. Inset: device structure. (b) Rise and fall times at 1 kHz. (c) "OR" gate logic. (d) "AND" gate logic with circuit diagrams ($V = 0$ V). (e) Target image schematic. (f) Imaging results (310×330 pixels) under 440–980 nm illumination.[92]

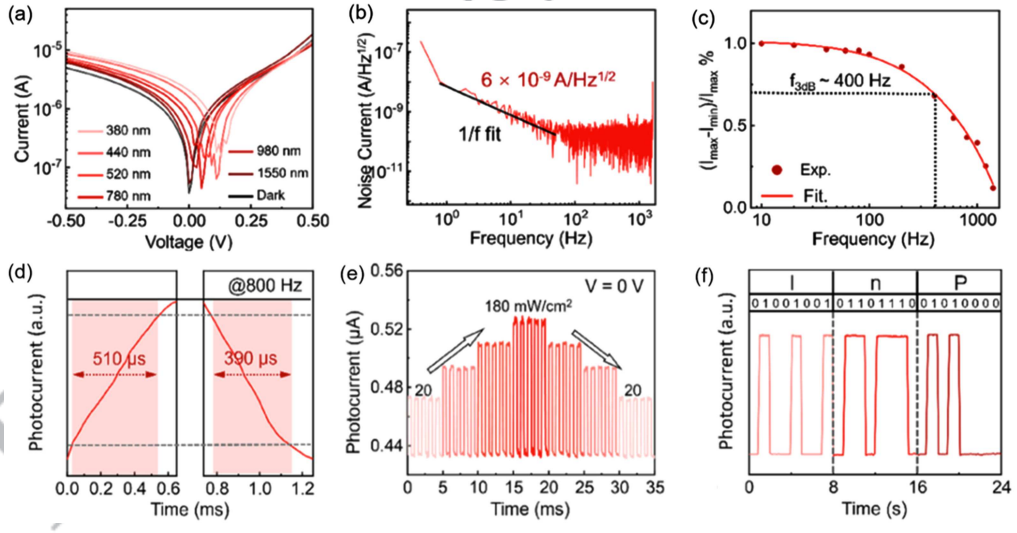


Fig. 12. (a) *I*–*V* characteristics of the 3D-graphene/InP photodetector at specific wavelengths. (b) Frequency-dependent noise current. (c) Photocurrent amplitude attenuation at various modulation frequencies. (d) Response time. (e) Photoresponse to varying optical power at 0 V bias. (f) Output signal of "InP" ASCII.[55]

3.2. N-doped 3D-graphene-based photodetectors

To enhance the interfacial band structure of the 3D-graphene/Si Schottky heterojunction, Zhang *et al.*[54] utilized PECVD to grow N-doped 3D-graphene *in situ* on a Si substrate, constructing an N-doped 3D-graphene/Si heterojunction photodetector. The N-doping modulated the Fermi level and reduced the Schottky barrier height of the 3D-graphene, which increased the built-in electric field strength. This modification facilitated the separation of photogenerated carriers, leading to dark current suppression and photocurrent enhancement. As shown in Figs. 13(a)–13(c), the device demonstrated a photoresponse across a spectrum of wavelengths, exhibiting a remarkably low dark current on the order of 10^{-11} A, a responsivity of 79.6 A/W, and a specific detectivity peaking at 10^{13} Jones, with response times recorded at 130 μs and 180 μs. Additionally, the device was capable of performing light-controlled "AND/OR" logic operations, enabling ASCII-encoded infrared communication and broadband imaging across the range of 440–1550 nm under 0 V bias, as depicted in Figs. 13(d)–13(f), demonstrating its application potential in the integration of photodetection, logic operations, and image sensing.

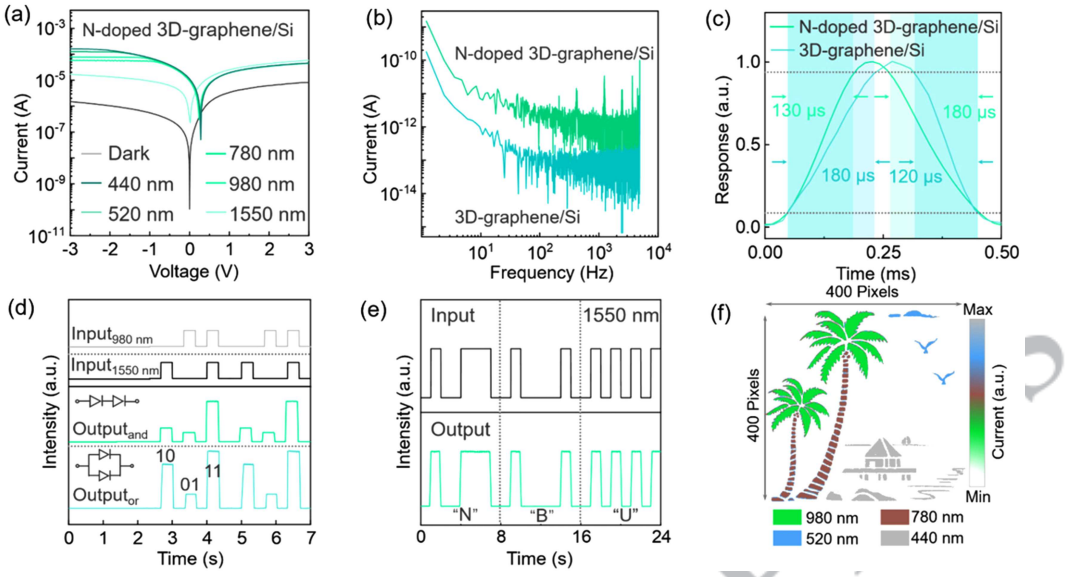


Fig. 13. (a) *I*–*V* curves of the N-doped 3D-graphene/Si photodetector at various light wavelengths. (b) Noise current comparison between two photodetectors. (c) Enlarged photoresponse curve at 2 kHz showing fast rise and fall times. (d) Input/output signals of light-controlled "AND" and "OR" gates. (e) Input/output signals for transmitting ASCII code "NBU" in infrared communication. (f) High-resolution 2D current mapping from 440 nm to 980 nm illumination.[54]

3.3. Engineering interfaces for controlled 3D-graphene-based photodetectors

While doping can enhance the performance of devices, significant challenges such as high interfacial recombination rates and elevated leakage currents continue to arise when 3D-graphene interfaces directly with semiconductor materials. To address these issues, the incorporation of an interfacial blocking layer has emerged as a critical strategy for optimizing device efficiency.[96] This approach leverages selective quantum tunneling and photovoltage-driven processes to achieve dark-state carrier blocking and facilitate efficient charge transport under illumination, mitigating dark currents and improving overall detection performance.[97–99]

In this context, He *et al.*[76] proposed a novel architecture by inserting a high dielectric constant tunneling layer between the 3D-graphene and the semiconductor, resulting in the construction of a thin high-κ photodetector (THPD). As shown in Figs. 14(a)–14(c), under the experimental condition of 1550 nm wavelength and −3 V bias, the device demonstrates a responsivity of 11.2 A/W, a specific detectivity of 5.9×10^{10} Jones, and response times of 168/196 μs. The implementation of the high-κ interfacial layer suppresses interfacial recombination and leakage currents, while simultaneously ensuring rapid carrier transport. This balance enhances both the sensitivity and response times of the device, underscoring its potential for applications in short-wave infrared communication and sensing technologies.

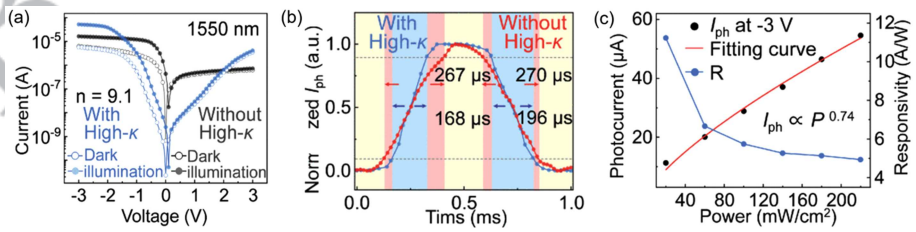


Fig. 14. (a) *I*–*V* curves of the HPD (black line) and THPD (blue line). (b) Enlarged view of a single on/off cycle for THPD and HPD. (c) I_{ph} (red) and R (blue) of THPD as a function of incident light power.[76]

3.4. QDs integrated 3D-graphene-based photodetectors

QDs offer tunable band gaps and enhanced light absorption capabilities, addressing Si's limitations in the near-infrared spectrum. Their ability to facilitate carrier trapping extends carrier lifetimes.[65–68] The porous structure[35,36] and exceptionally high specific surface area of 3D-graphene create a dense platform for QD integration, forming a highly efficient carrier injection interface.[63,64] This combination leverages a dual synergy of enhanced light absorption and interface modulation.

To mitigate the challenges of low light absorption efficiency and short carrier lifetimes in Si-based graphene photodetectors, Wu *et al.*[100] developed a MoS_2 QDs/3D-graphene/Si heterojunction photodetector. As shown in Figs. 15(a)–15(c), the device demonstrates an ultra-broadband response from 380 nm to 2200 nm, achieving a responsiv-

ity of 0.04 A/W, a specific detectivity of 1.15×10^{9} Jones, and response times of 300 μs and 280 μs. Figures 15(d)–15(f) present the output of encrypted information, specifically the letters "NIR", along with the responses of light-controlled logic gates ("AND" and "OR" gates) to light excitation at various wavelengths.

Lian *et al.*[101] developed a heterojunction composed of WS_2 QDs/3D-graphene/Si heterojunction. As illustrated in Fig. 16(a), the integration of WS_2 QDs markedly curtails carrier recombination, enhances charge separation, and results in a substantial increase in photocurrent. The temperature-dependent *I–V* characteristics at 1550 nm (across 243–373 K) depicted in Fig. 16(b) affirm that the device exhibits robust operational stability throughout a broad temperature spectrum. The response times recorded in Fig. 16(c) are impressively rapid at 139/145 μs, indicating an ultrafast dynamic response. Operating in a self-powered mode, the device achieves a responsivity of 83 A/W alongside a specific detectivity of 5.6×10^{11} Jones. As shown in Fig. 16(d), the self-powered photodetector can encrypt and process intricate binary signals under 1550 nm laser excitation. Furthermore, Figs. 16(e) and 16(f) reveal the outputs of light-controlled logic gates, specifically "AND" and "OR", through the application of dual-wavelength inputs. These advancements facilitate efficient optical signal encryption and the execution of logic operations, thereby paving the way for enhanced optical computing and information processing capabilities.

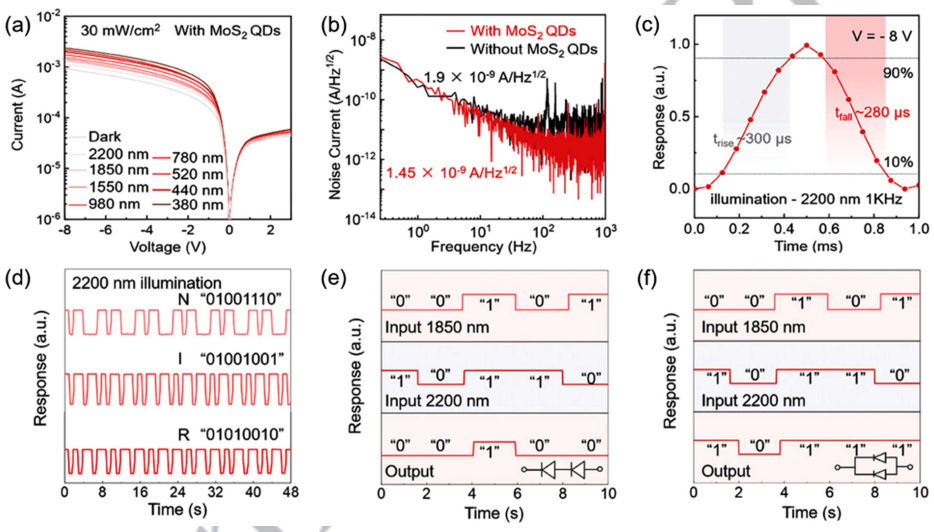


Fig. 15. (a) Optical response of MoS_2 QDs/3D-graphene/Si Schottky photodetectors. (b) Noise currents comparison of 3D-graphene/Si Schottky heterojunctions vs. MoS_2 QDs/3D-graphene/Si structures. (c) Device rise/fall times. (d) Encrypted information output at 2200 nm. (e) and (f) Logic gate responses ("AND" and "OR") to optical excitation at various wavelengths, with signal flow diagrams for the circuits.[100]

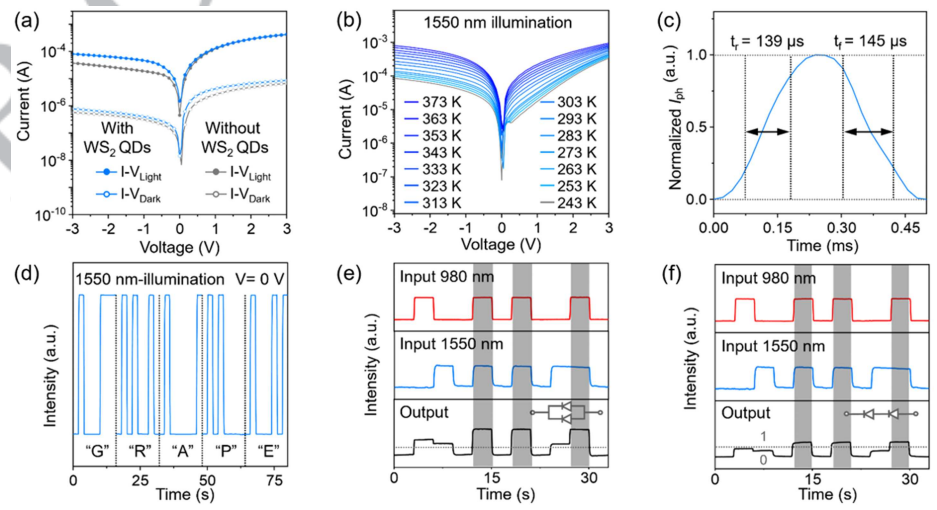


Fig. 16. (a) *I–V* curves of WS_2 QDs before and after integration with the 3D-graphene/Si Schottky heterojunction under dark and 1550 nm illumination. (b) *I–V* characteristics from 243 K to 373 K under 1550 nm illumination. (c) Rise and fall times of photodetectors. (d) Encrypted output from the device at 1550 nm. (e) Output response of the "OR" gate with different light excitations. (f) Output response of the "AND" gate with different light excitations.[101]

Zhang *et al.*[102] designed a C_3N QDs/3D-graphene/Si all-carbon framework photodetector assisted by machine learning. The D_{6h} symmetric structure of C_3N QDs reduces the carrier transport barrier at the 0D–3D carbon interface and improves the interfacial charge transfer efficiency. Figure 17(a) demonstrates that the device achieves a broadband response from 380 nm

to 1550 nm. The transient photocurrent (TPC) decay curves in Fig. 17(b) compare the carrier dynamics with and without C_3N QDs, and the inset shows the electrochemical impedance spectroscopy (EIS) Nyquist plot and equivalent circuit model, revealing the interfacial charge transfer capability. At 0 V, the device achieves a responsivity of 75.7 A/W, a specific detectivity of 1.23×10^{11} Jones, and response times of 257/296 μs (Fig. 17(c)). In addition, this device successfully implements dual-band logic operations, Morse code communication, and broadband image recognition capabilities, as shown in Figs. 17(d)–17(f), illustrating the significant potential of all-carbon optoelectronic devices in advanced intelligent information processing applications.

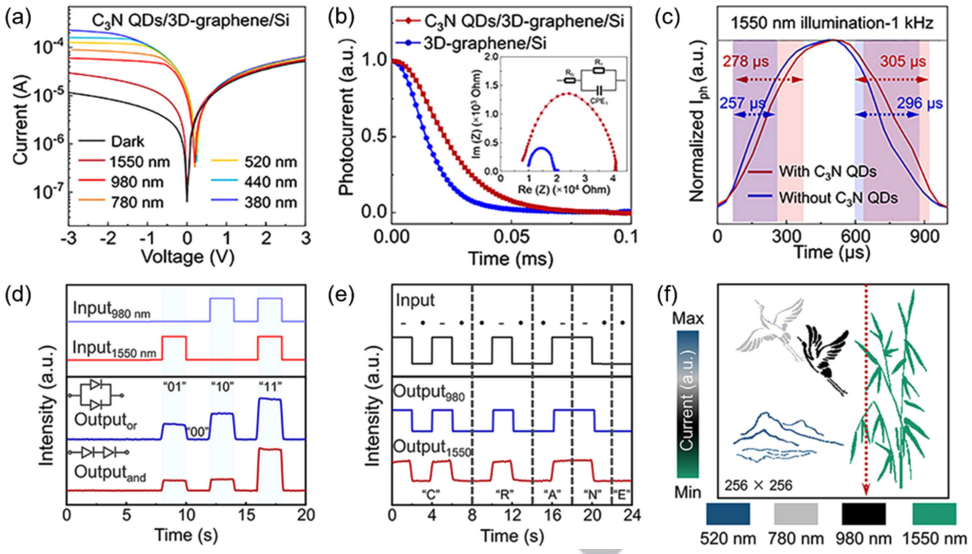


Fig. 17. (a) Broadband photoresponse of the C_3N QDs/3D-graphene/Si photodetector (380 nm to 1550 nm). (b) TPC and EIS Nyquist plot. (c) Response times of the photodetectors at 1550 nm and 1 kHz. (d) Responses of optical logic gates ("AND" and "OR") at 980 nm and 1550 nm. (e) Input/output signals for transmitting Morse code "CRANE" in an infrared system. (f) Image recognition results under various laser wavelengths (520 nm, 780 nm, 980 nm, and 1550 nm).[102]

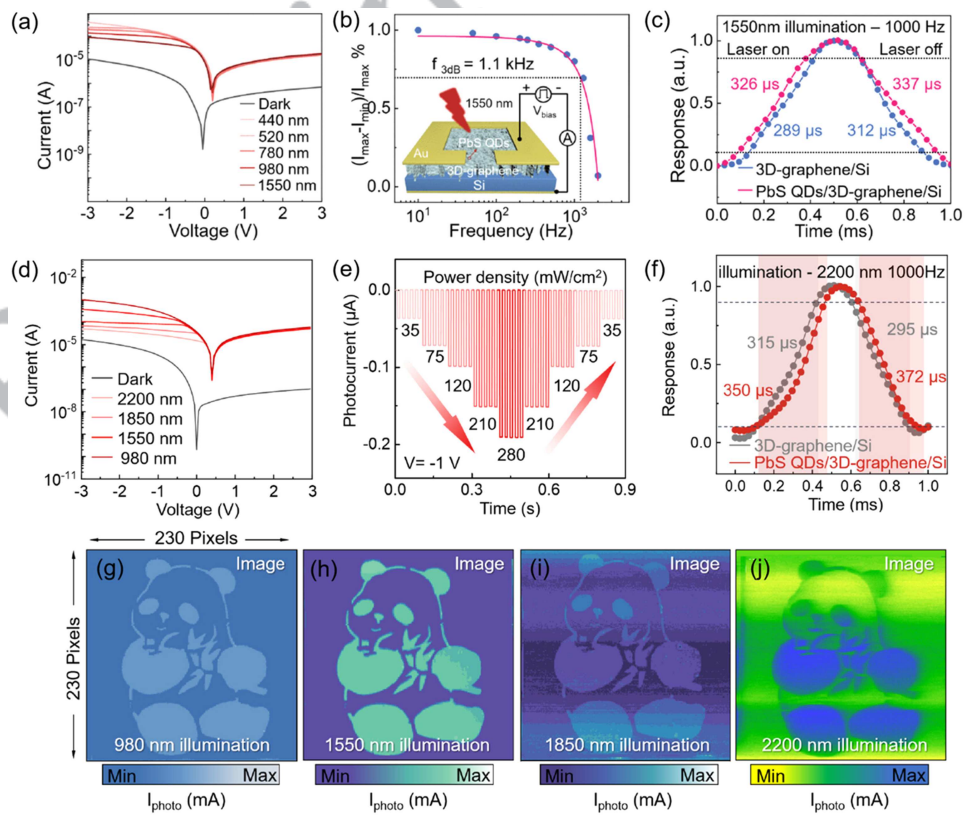


Fig. 18. (a) *I–V* curves of the device at various wavelengths (440 nm, 520 nm, 780 nm, 980 nm, and 1550 nm) with consistent light intensity. (b) Photocurrent amplitude attenuation at different modulation frequencies, with a schematic of the fabricated PD inset. (c) Enlarged photoresponse curves of PDs before and after 3D-graphene/Si heterojunction modification with PbS QDs at 1 kHz.[70] (d) *I–V* curves at the same intensity for different wavelengths. (e) PD response characteristics under 2200 nm illumination with −1 V reverse bias. (f) Rise/fall times of the PD under 2200 nm. (g)–(j) Imaging results of the "panda" pattern (230×230 pixels) under infrared (980–2200 nm) illumination.[71]

PbS QDs are gaining significant traction in long-wave near-infrared detection due to their narrow bandgap properties. Zhang *et al.*[70] constructed a PbS QDs/3D-graphene/Si heterojunction that utilizes the Fermi level difference between PbS QDs and 3D-graphene to enhance the built-in electric field, improving the separation efficiency of photogenerated carriers. As depicted in Figs. 18(a)–18(c), the device achieves a responsivity of 13.7 A/W and a specific detectivity of 1×10^{11} Jones at 1550 nm, with response times of 326/337 μs. Following further optimization, the device's detection capability extends to 2200 nm, maintaining a responsivity of 52 A/W and a specific detectivity of 6.8×10^{10} Jones, as shown in Figs. 18(d)–18(f). The infrared imaging results in Figs. 18(g)–18(j) verify its application potential in fields such as night vision surveillance, medical diagnosis, and infrared imaging.[71]

3.5. Optical-field modulation 3D-graphene-based photodetectors

3D-graphene has advantages like nanocavity architecture and strong optical field enhancement, but it has limitations in near-infrared light absorption. To address this, the incorporation of plasmonic nanostructures, micro/nano patterns, and optical resonant cavities can bolster the localized electromagnetic field. This enhancement allows for the effective recapture of "escaped" photons, leading to improved light absorption efficiency and increased carrier generation, ultimately elevating the optoelectronic performance of the device.[103–105]

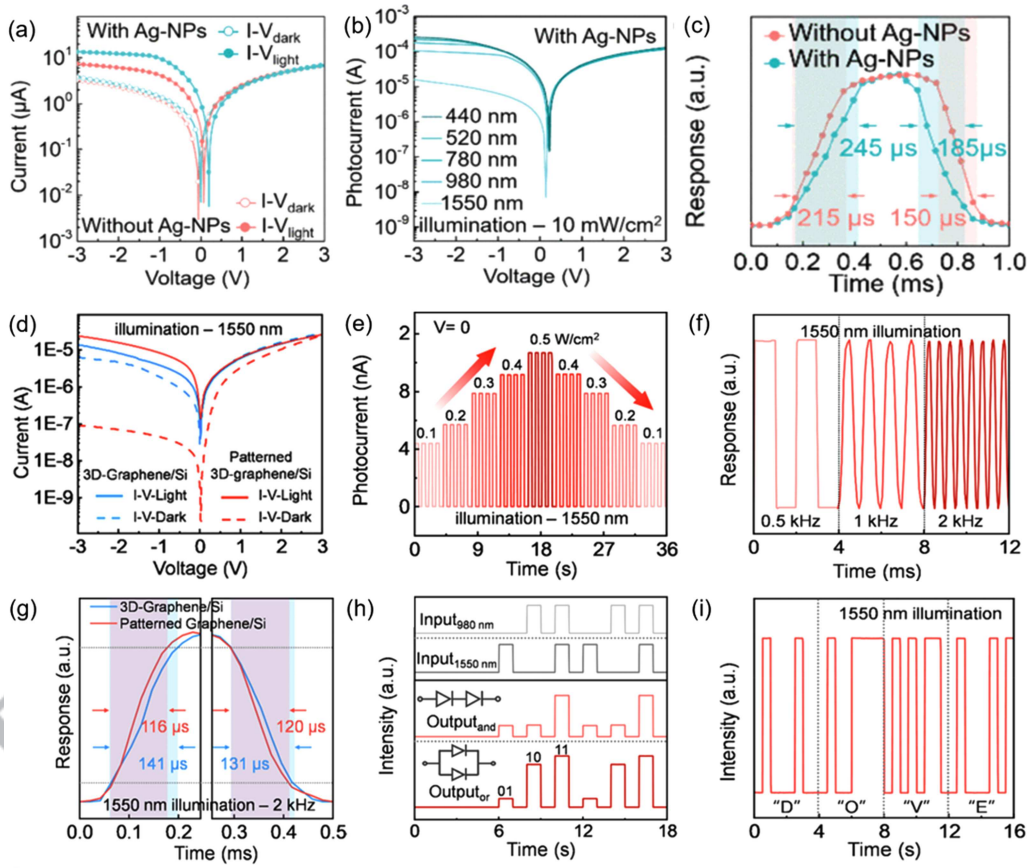


Fig. 19. (a) *I*–*V* curves under dark/light conditions. (b) I_{ph}–*V* curves for different illumination wavelengths. (c) Enlarged photoresponse curve at 1 kHz.[72] (d) Comparison of *I*–*V* characteristics for patterned vs. unpatterned photodetectors under dark and 1550 nm illumination. (e) Photocurrent characteristics of patterned 3D-graphene/Si photodetectors at 1550 nm (0 V). (f) Light response of patterned 3D-graphene/Si photodetectors under frequency modulations. (g) Enlarged response curve at 2 kHz showing rise/fall times. (h) *I*–*T* curves of dual-band optoelectronic logic gates with "OR" and "AND" circuit diagrams. (i) Output signals of "DOVE".[108]

LSPR plays a crucial role in facilitating optical field coupling.[106,107] When the oscillation frequency of free electrons in metal nanoparticles aligns with the incident light frequency, a pronounced localized electric field emerges, enhancing light absorption. Zhang *et al.*[72] integrated Ag-NPs into a 3D-graphene/Si heterojunction to construct a near-infrared photodetector. As shown in Figs. 19(a)–19(c), a significant improvement in both dark current and photocurrent was demonstrated, extending the detection wavelength to 1550 nm, achieving a responsivity of 65.3 A/W, a specific detectivity of 1.5×10^{10} Jones, and response times of 245/185 μs, indicating that the LSPR effect enhances near-infrared light absorption and carrier transport. Furthermore, micro/nano-patterned structures have been shown to optimize optical field distribution. Wang *et al.*[108] fabricated a patterned 3D-graphene/Si photodetector that boosts localized optical fields and modulates carrier transport through structural design. As shown in Figs. 19(d) and 19(e), compared to

conventional 3D-graphene/Si, the patterned variant exhibited a lower dark current and a higher photocurrent, achieving a responsivity of 68.47 A/W and a specific detectivity of 1.43×10^{12} Jones under self-powered conditions at 0 V, with response times of 116/120 μs (Figs. 19(f) and 19(g)). Figures 19(h) and 19(i) demonstrate that the device enables dual-band optical logic operations and binary-encoded communication, highlighting its prospective applications in high-speed optical communication and information processing.

Furthermore, Zhang *et al.*[109] employed a curvature-induced localized photonic resonance (CLPR) mechanism to enhance optical field interactions and developed a 3D-graphene/Si photodetector. The curvature-induced structure strengthens the electromagnetic field confinement in localized regions, leading to improved near-infrared photoresponse characteristics. As shown in Figs. 20(a)–20(c), the CLPR device exhibits a lower dark current and a higher on/off ratio at 1550 nm, achieving a responsivity of 11 A/W, a specific detectivity of 1.07×10^{11} Jones, and fast response times of 267/260 μs. Figures 20(d) and 20(e) demonstrate the device's capabilities in 1550 nm communication encoding and multi-wavelength image recognition, emphasizing its potential for high-speed near-infrared communication and advanced imaging systems.

In addition to the benefits provided by micro-nano structures, substrate optical cavities play a crucial role in enhancing optical field coupling. Specifically, the buried oxide layer in SOI substrates can establish an optical resonant cavity that reflects unabsorbed light back into the active region, thereby facilitating multiple optical path enhancements.[110–112] He *et al.*[73] constructed a 3D-graphene/SOI broadband photodetector. As shown in Figs. 21(a)–21(d), the device exhibits excellent photoresponse across a wide spectral range. At 1550 nm, it achieves a responsivity of 27.4 A/W, a specific detectivity of 1.37×10^{11} Jones (at −0.5 V), and response times of 212/242 μs, along with good stability and reproducibility. The synergistic effect between the SOI optical cavity and the 3D-graphene nanocavity structure enhances the light–matter interaction, providing a new design concept for low-cost, high-performance integrated optoelectronic devices.

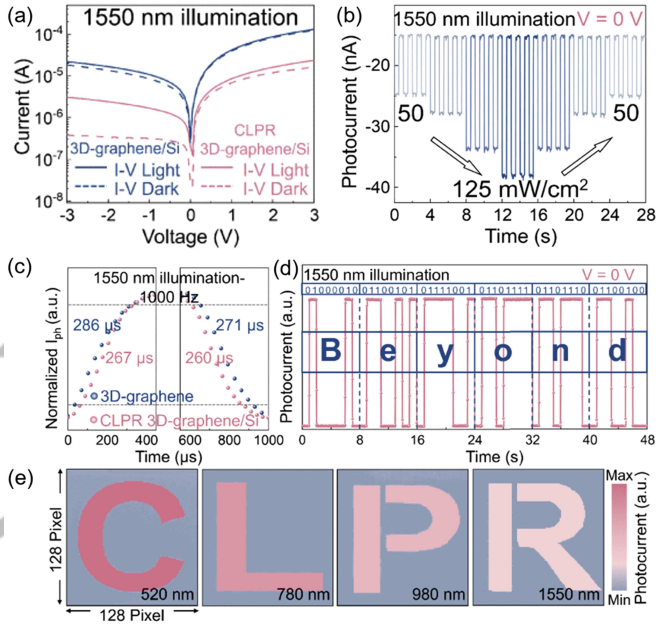


Fig. 20. (a) *I–V* curves of 3D-graphene/Si Schottky and CLPR 3D-graphene/Si photodetectors under 1550 nm illumination and in the dark. (b) Optical power response of the CLPR 3D-graphene/Si photodetector at 1550 nm with 0 V bias. (c) Response time of photodetectors. (d) Output signal from "Beyond" ASCII code with a 1550 nm laser. (e) Image recognition results with lasers at 520 nm, 780 nm, 980 nm, and 1550 nm.[109]

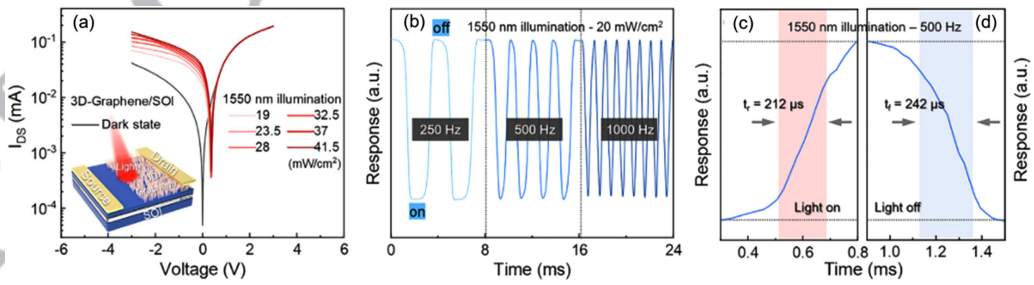


Fig. 21. (a) *I–V* curves for a device irradiated with 1550 nm light at various intensities, with a schematic of the 3D-graphene/SOI device inset. (b) Photoresponse of the device to light (1550 nm) at 250 Hz, 500 Hz, and 1000 Hz. (c) and (d) Enlarged images of the photoresponse at 500 Hz showing fast rise and fall times.[73]

3.6. 3D-graphene-based flexible sensors

The devices discussed are mainly fabricated on rigid substrates, which inherently restrict their flexibility and application scope. In contrast, the vertically interconnected porous network of 3D-graphene presents considerable structural benefits for flexible device integration.[113] This material maintains high electrical conductivity while its hierarchical pore architecture enhances the specific surface area and allows for versatile interface modulation.[114] During mechanical deformation, such as bending or stretching, the 3D conductive framework regulates stress distribution, influencing the electrostatic potential and electromagnetic coupling at the heterointerface.[115] By utilizing various flexible substrates, these structural advantages can be harnessed to enable multi-dimensional functionalities, including photodetection and mechanical sensing.

3.6.1. 3D-graphene/PDMS flexible sensor

The integration of 3D-graphene with a flexible polymer substrate enables direct modulation of the conductive contact state within its porous network through applied strain, resulting in a measurable change in resistance that facilitates real-time human motion monitoring.[116] The 3D-graphene/polydimethylsiloxane (PDMS) system exhibits an anisotropic conductive architecture, granting the device omnidirectional strain sensing capabilities.

In the 3D-graphene/PDMS composite, the device possesses combined optoelectronic and mechanical response functionalities.[117] Tensile testing reveals a pronounced directional dependence in its response characteristics (Fig. 22(a)). The pressure response time is approximately 0.7 s, while the recovery phase is influenced by the intricacies of the porous structure, yielding a relaxation time of 4.41 s (Fig. 22(b)). During dynamic monitoring, the device differentiates between various motion states, such as walking, running, and jumping (Fig. 22(c)), displaying distinct signal profiles. It can be utilized for monitoring physiological cues such as blinking, facial expressions, respiration, and joint movements. This capability highlights its potential applications in health monitoring, human–machine interaction, and rehabilitation training, along with demonstrating deformation adaptability and stability.

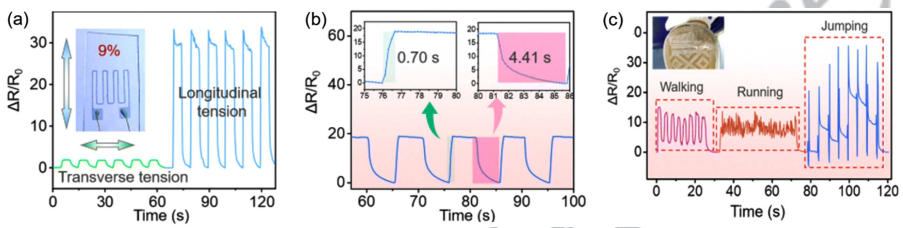


Fig. 22. (a) Response evaluation of the 3D-graphene flexible sensor in various stretching directions. (b) Response time measurement. (c) Sensor used on the sole to detect walking, running, and jumping signals.[117]

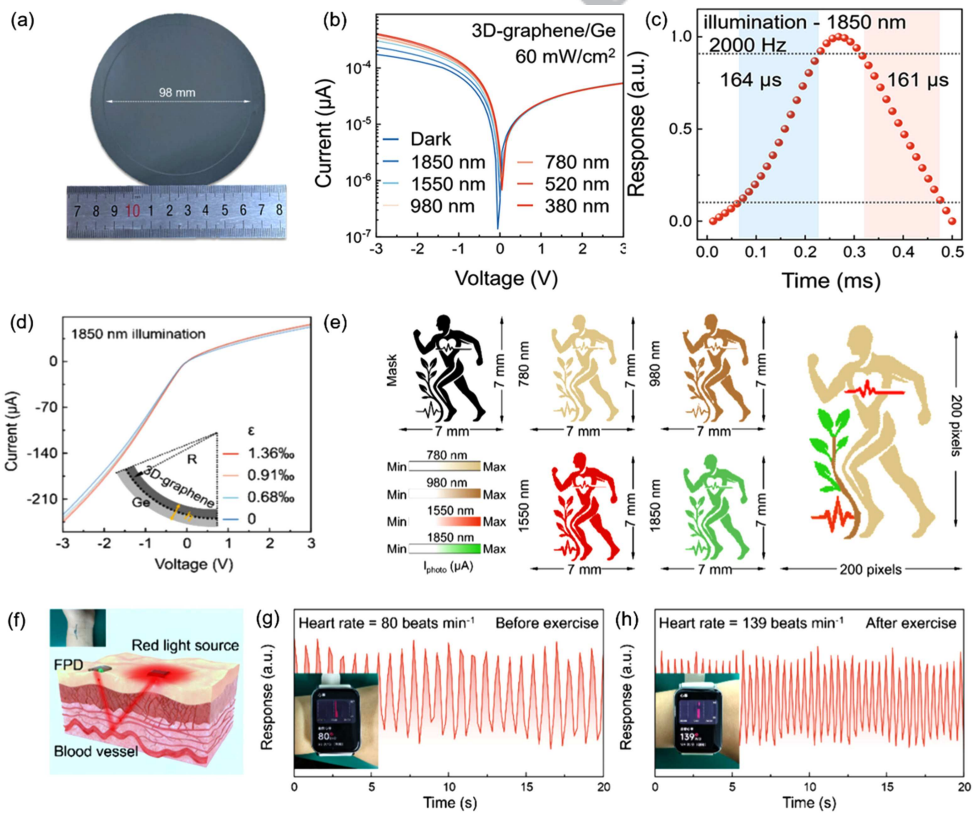


Fig. 23. (a) Photo of a 4-in wafer-scale flexible Ge film. (b) *I–V* characteristics of the flexible 3D-graphene/Ge heterojunction at different wavelengths. (c) Rise and fall times. (d) *I–V* characteristics under strain at 1850 nm. (e) Mask pattern for imaging tests and multi-wavelength photocurrent distribution images. (f) Wrist-based detection configuration for heart rate measurements on (g) resting and (h) post-exercise conditions.[125]

3.6.2. 3D-graphene/Ge flexible sensor

In flexible semiconductor systems, the incorporation of 3D-graphene converts the non-uniform strain from mechanical bending into interfacial coupling phenomena. This interaction synergistically modulates the stress field, electrostatic potential, and carrier transport, thereby enhancing the optoelectronic response under strain conditions.[118–124] A flexible photodetector built on a 3D-graphene/Ge heterostructure demonstrates a remarkable broadband spectral response.[125] The narrow bandgap of Ge (0.67 eV) enables the device to op-

erate across a wavelength range of 380–1850 nm, exhibiting exceptional optoelectronic performance metrics (Figs. 23(a)–23(c)), including a responsivity of 80.2 A/W, a specific detectivity of 1.2×10^{11} Jones, response times of 164/161 μs, and a cutoff frequency of 1.8 kHz. The device maintains a stable response across varying bending strains and presents tunable characteristics (Fig. 23(d)). Application demonstrations indicate the potential for multi-wavelength imaging, facilitating target recognition and image fusion at wavelengths of 780 nm, 980 nm, 1550 nm, and 1850 nm (Fig. 23(e)). Furthermore, integration into wearable technology enables heart rate photoplethysmography (PPG) monitoring during both resting and exercise conditions (Figs. 23(f)–23(h)), paving new avenues for the development of advanced flexible optoelectronic devices and biosensing applications.

4. Summary

This review summarizes advancements in 3D-graphene-based photodetectors, highlighting material properties, heterostructure design, and performance modulation strategies. Key methods include semiconductor heterostructure construction, nitrogen doping, interface optimization, quantum dot composites, and flexible integration, greatly enhancing optoelectronic features. The spectral response has expanded from ultraviolet to short-wave infrared (380–2200 nm), with responsivity reaching 83 A/W, specific detectivity of 10^{13} Jones, and a reduced response time of 116 μs. These devices are self-powered, stable over a wide temperature range, and suitable for applications like broadband imaging, high-speed optical communication, and wearable electronics. The photodetection mechanisms rely on the built-in electric field of the Schottky heterojunction for effective carrier separation and transport. Key performance metrics are summarized in Table 1, showing the versatility of these devices in various applications, including infrared communication and biosensing. Moreover, growing 3D-graphene on semiconductor substrates improves adhesion and compatibility, paving the way for integrated optoelectronic systems.

Table 1. Performance metrics for 3D-graphene photodetectors, including responsivity, response time, wavelength, and detectivity.

Device structure	Wavelength (nm)	t_r (μs)	t_f (μs)	Responsivity (A/W)	Detectivity (Jones)	Ref.
Seaweed photonic graphene/Si	1550	130	154	82	1.1×10^{11}	[83]
VAGNAS/Si	1550	178	186	66	7.3×10^{10}	[90]
3D-graphene/GaAs	980	302	295	3.1	1×10^{10}	[92]
3D-graphene/InP	1550	510	390	12.2	2.1×10^{10}	[55]
N-3D-graphene/Si	1550	130	180	79.6	1.4×10^{13}	[54]
3D-graphene/high-κ/Si	1550	168	196	11.2	5.9×10^{10}	[76]
MoS_2 QDs/3D-graphene/Si	2200	300	280	0.04	1.15×10^{9}	[100]
WS_2 QDs/3D-graphene/Si	1550	139	145	83	5.6×10^{11}	[101]
C_3N QDs/3D-graphene/Si	1550	257	296	75.7	1.23×10^{11}	[102]
PbS QDs/3D-graphene/Si	1550	326	337	13.7	1×10^{11}	[70]
PbS QDs/3D-graphene/Si	2200	350	372	52	6.8×10^{10}	[71]
Ag-NPs/3D-graphene/Si	1550	245	185	65.3	1.5×10^{10}	[72]
Patterned 3D-graphene/Si	1550	116	120	68.47	1.43×10^{12}	[108]
CLPR 3D-graphene/Si	1550	267	260	11	1.07×10^{11}	[109]
3D-graphene/SOI	1550	212	242	27.4	1.37×10^{11}	[73]
3D-graphene/Ge	1850	164	161	80.2	1.2×10^{11}	[125]

5. Outlook and challenges

While considerable advancements have been made in the development of 3D-graphene photodetectors, several hurdles must be addressed to transition these technologies into next-generation high-performance photodetection applications. This section outlines potential opportunities for emerging photodetection technologies, focusing on scalable synthesis, optoelectronic integration, innovative architectures, and commercialization pathways.

5.1. Scalable synthesis and optoelectronic system integration

To achieve controlled synthesis of high-quality 3D-graphene, it is crucial to optimize various PECVD parameters in a coordinated manner tailored to specific functions. Growth temperature plays a key role in enhancing the surface diffusion of reactive carbon species and fostering sp^2-lattice reconstruction to improve crystallinity while minimizing amorphous carbon formation. Both plasma power and working pressure influence precursor dissociation, reactive-species density, and the intensity of ion bombardment; thus, establishing an optimal processing window is vital to encourage vertical nanosheet growth while reducing plasma-induced defects. When CH_4 serves as the carbon precursor, the presence of H_2 can selectively etch weakly bonded and amorphous carbon, making the CH_4/H_2 flow ratio critical in balancing carbon deposition with etching processes. This balance is essential in regulating nucleation density, intersheet spacing, and edge density, while the duration of growth mainly determines the height of nanosheets and the connectivity of the network.

CPB Online In-Press

Through coordinated optimization, one can fine-tune porosity and network connectivity, enhancing light trapping capabilities while ensuring efficient carrier transport.

On the integration front, device architecture and interface configuration should be synergistically considered alongside heterogeneous integration. Combining 3D-graphene with semiconductors, 2D materials, quantum dots, and ultrathin dielectric layers allows for the precise tuning of band alignment, mitigating dark current and interfacial recombination while broadening spectral response. However, the presence of exposed edges and complex interfaces heightens susceptibility to environmental degradation, making encapsulation and reliability enhancements critical. Future encapsulation techniques must guard against oxygen and moisture ingress without compromising the porous configuration or hindering optically and electrically active interfaces. For comprehensive systems, strategies such as low-temperature processing, selective-area growth, pixel-array fabrication, readout integration, and waveguide coupling will be pivotal in developing CMOS-compatible on-chip systems. Additionally, the integration of mechanically robust encapsulation, stretchable interconnects, and signal-decoupling measures will facilitate the progression of flexible and wearable optoelectronic devices.

5.2. Advanced architectures and process integration

In addition to periodic enhancements of existing structures, several innovative architectures from the broader photodetector domain could be repurposed to exploit the distinct characteristics of 3D-graphene. (i) Unipolar barrier architectures for dark-current suppression. Implementing a unipolar barrier can effectively limit majority-carrier injection while enabling photocarrier extraction, thus reducing dark current and potentially increasing specific detectivity without significant trade-offs on photoresponse.[126] This approach could be advantageous for 3D-graphene/Si Schottky photodetectors, where thermionic emission-related dark current constrains performance. Techniques such as work-function modulation via N-doping or interface engineering, combined with interfacial band engineering, can establish asymmetrical carrier-selective barriers while facilitating photocarrier transport through the porous network. (ii) Dual-band photodetectors for multispectral discrimination. The inherent broadband response of 3D-graphene/Si heterojunctions allows for multiwavelength detection,[127] yet lacks built-in spectral discrimination. Inspired by vertically stacked back-to-back architectures,[128] a dual-band device could leverage the visible to near-infrared interband absorption of Si alongside the internal photoemission facilitated by 3D-graphene below the Si bandgap as distinct spectral channels. Achieving independent carrier extraction and minimizing spectral crosstalk will necessitate oppositely directed built-in fields or carrier-selective barriers, enabling filter-free dual-band discrimination. (iii) Integrating with Si photonic waveguides is critical for enabling on-chip optical communication.[129] The unique properties of 3D-graphene offer a significant advantage in this context, facilitating innovative developments in on-chip optical interconnections.[23] Through these targeted strategies and advanced architectures, 3D-graphene photodetectors have the potential to significantly impact the future landscape of photodetection technologies.

5.3. Commercialization pathways

Scalable manufacturing and performance uniformity: Successful commercialization hinges on achieving wafer-scale control over pivotal parameters such as nanosheet height, intersheet spacing, porosity, edge density, and defect concentration. These characteristics significantly influence optical absorption, carrier transport, and photoelectric conversion efficiency. Large-area fabrication techniques must minimize spatial variations and device-to-device as well as batch-to-batch inconsistencies to attain performance metrics on par with established commercial photodetectors.

Process compatibility: The growth and processing methodologies for 3D-graphene diverge significantly from traditional semiconductor fabrication techniques. Notably, the high temperatures and plasma bombardment associated with PECVD can compromise the integrity of semiconductor surfaces, dielectric materials, and pre-existing circuitry. Therefore, it is crucial to develop low-temperature, low-damage, and selective-area growth techniques that are compatible with standard lithography processes, metal interconnections, passivation layers, and back-end-of-line manufacturing.

Long-term stability and packaging reliability: The porous architecture and exposed edges of 3D-graphene make it vulnerable to moisture, oxygen, and various environmental contaminants, which can lead to fluctuations in work function, interfacial barrier height, dark current, and photoresponse. To mitigate these issues, conformal encapsulation methods that maintain the integrity of the porous structure and active interfaces, along with rigorous environmental and operational aging assessments, are essential to ensure lasting stability and reproducibility in performance.

Acknowledgements

This study was supported by the National Natural Science Foundation of China (Grant Nos. 12474273 and 62204133), the Open Research Fund of China State Key Laboratory of Materials for Integrated Circuits (Grant No. SKLJC-K2025-06), Ningbo Youth Leading Talent Project (Grant No. 2024QL013), and the Ningbo Natural Science Foundation (Grant No. 2024J148).

CPB Online In-Press

References

[1] Teng F, Hu K, Ouyang W X and Fang X S 2018 *Adv. Mater.* **30** 1706262
[2] Liu X, Deng C Y, Wei H, Fang M K, Yan B, Zhu T, Luo S, Peng G, Cai W W, Long M S and Zhang X A 2025 *Adv. Funct. Mater.* **35** 2423102
[3] Wang B, Zhong S P, Xu P and Zhang H 2021 *Chem. Eng. J.* **403** 126336
[4] Yang B X, Gao W, Li H Y, Gao P, Yang M M, Pan Y, Wang C L, Yang Y N, Huo N J, Zheng Z Q and Li J B 2023 *Nanoscale* **15** 3520
[5] Li H Y, Huang J M, Gao P, Yang B X, Lan Z B, Gao W, Zhang F, Yang M M, Zheng Z Q, Huo N J and Li J B 2023 *IEEE Trans. Electron Devices* **70** 2358
[6] Xia X L, Zhou S Y, Wang Y and Zhang Z Y 2025 *Fundam. Res.* **5** 1153
[7] Huo N J and Konstantatos G 2018 *Adv. Mater.* **30** 1801164
[8] Wang J Y, Ling C C, Xue X, Ji H G, Rong C, Xue Q Z, Zhou P H, Wang C K, Lu H P and Liu W P 2024 *Small* **20** 2310107
[9] Bartolo-Perez C, Chandiparsi S, Mayet A S, Cansizoglu H, Gao Y, Qarony W, Ahamed A, Wang S Y, Cherry S R, Islam M S and Ariño-Estrada G 2021 *Opt. Express* **29** 19024
[10] Wang Z, Tan C H, Peng M, Yu Y Y, Zhong F, Wang P, He T, Wang Y, Zhang Z H, Xie R Z, Wang F, He S J, Zhou P and Hu W D 2024 *Light Sci. Appl.* **13** 277
[11] Xu H Y, Xu Z H, Ren Q Q, Meng Y, Han S, Wang Z Q, Chai Y, Bae S H and Hu W D 2026 *Nat. Mater.*
[12] Ge Y K, Huang Z W, Yang M H, Fang J H, Ke S Y, Liu G Z, Zhou J R, Chen J Q and Zhang H L 2026 *Appl. Surf. Sci.* **741** 167124
[13] Lan B F, Jin X F, Yang Z H, Wang J, Zhou W Y, Guan Y, Zhu J, Wang Z and Kan B 2026 *Mater. Horiz.* **13** 4421
[14] Huang H Q, Yang Y, Liu L, Mu F, Zhang W B, Huang Y F, Yang L J, Song F and Liu Y K 2026 *J. Mater. Chem. A* **14** 15918
[15] Nasr J R, Simonson N, Oberoi A, Horn M W, Robinson J A and Das S 2020 *ACS Nano* **14** 15440
[16] Zhao T G, Liu X, Ge X, Duan S K, Bai Y Z, Yu Y Y, Fu H R, Xu H Y, Gao L, Xu J B, Martyniuk P, Zhang L B, Wang Z and Hu W D 2026 *Nat. Commun.* **17** 7459
[17] Wang F, Zhang T, Xie R Z, Wang Z and Hu W D 2023 *Nat. Commun.* **14** 2224
[18] Yang D Z and Ma D G 2019 *Adv. Opt. Mater.* **7** 1800522
[19] Zhang X Y, Jing Q S, Ao S, Schneider G F, Kireev D, Zhang Z J and Fu W Y 2020 *Small* **16** 1902820
[20] Novoselov K S, Geim A K, Morozov S V, Jiang D, Zhang Y, Dubonos S V, Grigorieva I V and Firsov A A 2004 *Science* **306** 666
[21] Zhuo Z W, Wu X J and Yang J L 2020 *Nanoscale* **12** 19359
[22] Li P L, Wei W Y, Zhang M, Mei Y F, Chu P K, Xie X M, Yuan Q H and Di Z F 2020 *Nano Today* **34** 100908
[23] Koepfli S M, Baumann M, Koyaz Y, Gadola R, Gungor A, Keller K, Horst Y, Nashashibi S, Schwanninger R, Doderer M, Passerini E, Fedoryshyn Y and Leuthold J 2023 *Science* **380** 1169
[24] Zhao M H, Xue Z Y, Zhu W, Wang G, Tang S W, Liu Z D, Guo Q L, Chen D, Chu P K, Ding G Q and Di Z F 2020 *ACS Appl. Mater. Interfaces* **12** 15606
[25] Guan H Y, Hong J Y, Wang X L, Ming J Y, Zhang Z L, Liang A J, Han X Y, Dong J L, Qiu W T, Chen Z, Lu H H and Zhang H 2021 *Adv. Opt. Mater.* **9** 2100245
[26] Xie C, Mak C H, Tao X M and Yan F 2017 *Adv. Funct. Mater.* **27** 1603886
[27] Zhou T Y, Yang M, Wang J Y, Chen X, Yan Q Y, Watanabe K, Taniguchi T, Liu X, Huang Y Q, Xu W G, Wang X R, Gao L and Hu Z H 2025 *Adv. Electron. Mater.* **11** 2500001
[28] Huang J and Kang J 2022 *J. Phys.: Condens. Matter* **34** 165301
[29] Kaur M, Singh N K, Sarkar A, George S J and Rao C N R 2018 *ACS Appl. Nano Mater.* **1** 5101
[30] Peng M, Yu Y Y, Wang Z, *et al*. 2022 *ACS Photonics* **9** 1775
[31] Li P P, Wang T L, Wang A C, Zhao L, Zhu Y Q, Wang Z W, Gao H L, Wang W J, Li K L and Du C H 2024 *Appl. Surf. Sci.* **649** 159135
[32] Guo L, Han J Y and Wang J 2024 *J. Mater. Chem. C* **12** 1233
[33] Li S P, Lei T, Yan Z X, Wang Y, Zhang L K, Tu H Y, Shi W H and Zeng Z M 2024 *Chin. Phys. B* **33** 018501
[34] Li G Z, Huang B, Pan Z F, Su X Y, Shao Z P and An L 2019 *Energy Environ. Sci.* **12** 2030
[35] Hiramatsu M, Shiji K, Amano H and Hori M 2004 *Appl. Phys. Lett.* **84** 4708
[36] Han X G, Yang Z, Zhao B, Zhu S Z, Zhou L H, Dai J Q, Kim J W, Liu B Y, Connell J W, Li T, Yang B, Lin Y and Hu L 2017 *ACS Nano* **11** 3189
[37] Wang S, Wang X, Sun C L and Wu Z S 2021 *J. Energy Chem.* **61** 23
[38] Ma J H, Wang P, Dong L, Ruan Y B and Lu H B 2019 *J. Colloid Interface Sci.* **534** 12
[39] Mo Y C, Yang K C, Lin J S, Liu M T, Ye G F and Yu J 2023 *J. Mater. Chem. A* **11** 6349
[40] Higuchi T, Heide C, Ullmann K, Weber H B and Hommelhoff P 2017 *Nature* **550** 224
[41] Jiang J J, Zhou W T, Li W Y, Huang Z Y, Zhang M M, Jin J Y and Xie J M 2024 *Chem. Eng. J.* **496** 154123
[42] Zhang N, Jiang X J, Fan J, Luo W W, Xiang Y X, Wu W, Ren M X, Zhang X Z, Cai W and Xu J J 2019 *Nanotechnology* **30** 505201
[43] Zhang Y, Li Y N, You Q, Sun J Y, Li K, Hong H, Kong L B, Zhu M Q, Deng T and Liu Z W 2023 *Nanoscale* **15** 1402
[44] Wang H P, Li X B, Gao L, Wu H L, Yang J, Cai L, Ma T B, Tung C H, Wu L Z and Yu G 2018 *Angew. Chem. Int. Ed.* **57** 192
[45] Chen Z, Jin L, Hao W, Ren W C and Cheng H M 2019 *Mater. Today Nano* **5** 100027
[46] Wang H P and Yu G 2016 *Adv. Mater.* **28** 4956
[47] Shin D H and Choi S H 2018 *Micromachines* **9** 350
[48] Periyanagounder D, Gnanasekar P, Varadhan P, He J H and Kulandaivel J 2018 *J. Mater. Chem. C* **6** 9545
[49] He X, Wang Q, Shen M Y, Liu H, Wang J, Yuan X G, Zhang Y G, Liu K, Cai S W, Huang Y Q and Ren X M 2026 *Opt. Lett.* **51** 1295
[50] Li Y J, Zhao Y N, Ruocco A, Wang M Q, Li B and Akhavan S 2025 *ACS Appl. Mater. Interfaces* **17** 6716
[51] Fang Z N, Wang J H, Liu W H, Liang Z H, Pan Q B, Lu P, Cui B, Lu X, Jiang J, Li Y, Gu Z, Xiu P, Wang H F and Fang H P 2026 *Nat. Commun.* **17** 4339
[52] Peng K D, Cai Z Y, He J F and Huang Q D 2026 *Opt. Laser Technol.* **196** 114690
[53] Rashidi B, Mohammad Khani A A, Rezaei I, Soldoozy A and Aghaee T 2024 *Opt. Mater.* **148** 114819
[54] Zhang G L, Wang B K, Wu H J, Zhang J Q, Lian S S, Bai W J, Zhang S, Liu Z D, Yang S W, Ding G Q, Ye C C, Zheng L and Wang G 2024 *Nano Lett.* **24** 10062
[55] Zhang J Q, Xu Z Y, Zhu F H, Lian S S, Cao G Q, Ma H, Zheng L and Wang G 2025 *Appl. Phys. Lett.* **127** 032106
[56] Chen W W, Yang L Z, Wang P J, Zhang Y W, Zhou L Q, Yang T J, Wang Y and Yang J Y 2016 *Opt. Commun.* **372** 85
[57] Li C and Shi G Q 2012 *Nanoscale* **4** 5549
[58] Fang Q L, Shen Y and Chen B L 2015 *Chem. Eng. J.* **264** 753
[59] Peurifoy S R, Castro E, Liu F, Zhu X Y, Ng F, Jockusch S, Steigerwald M L, Echegoyen L, Nuckolls C and Sisto T J 2018 *J. Am. Chem. Soc.* **140** 9341
[60] Wang B K, Zhang J Q, Wu H J, Zhu F H, Lian S S, Cao G Q, Ma H, Hu X R, Zheng L and Wang G 2025 *J. Semicond.* **46** 071401
[61] Tang Y, Huang F, Bi H, Liu Z and Wan D 2012 *J. Power Sources* **203** 130
[62] Liu K W, Chen Y M, Policastro G M, Becker M L and Zhu Y 2015 *ACS Nano* **9** 6041
[63] Zhang S, Zhang G L, Liu Z D, He Z Y, Feng X Q, Yang S W, Ding G Q, Wang G and Wang Y Q 2022 *J. Mater. Chem. C* **10** 11874
[64] D'Apuzzo F, Piacenti A R, Giorgianni F, Autore M, Guidi M C, Marcelli A, Schade U, Ito Y, Chen M W and Lupi S 2017 *Nat. Commun.* **8** 14885
[65] Shih J A, Yang S J, Chen C Y, Sone M, Chang T F M, Pu Y C and Hsu Y J 2025 *ACS Appl. Nano Mater.* **8** 8154
[66] Mokkath J H 2021 *Int. J. Quantum Chem.* **121** e26763
[67] Shultz A, Gong M, Maroufian S A, Takacs F and Wu J Z 2026 *Adv. Opt. Mater.* **14** e03700
[68] Han Z Y, Liu X, Lu Z Q, Zheng Y, Zhang B X, Meng T, Zhang H, Liu M, Li J, Zhang L and Sun B 2026 *J. Phys. Chem. Lett.* **17** 3205
[69] Hou X Q, Kang J, Qin H Y, Chen X W, Ma J L, Zhou J H, Chen L P, Wang L J, Wang L W and Peng X G 2019 *Nat. Commun.* **10** 1750
[70] Zhang S, Zhang G L, Zheng L, Liu Z D, Wang B K, Wu H J, He Z Y, Jin Z W and Wang G 2023 *IEEE Electron Device Lett.* **44** 1240
[71] Wu H J, Liu Z Y, Wang B K, Zheng L, Lian S S, Zhang J Q, Zhang S, Zhang G L, Xue Z Y, Yang S W, Cheng X, Ding G Q, Liu Z D, Ye C C and Wang G 2024 *ACS Photonics* **11** 1342
[72] Zhang G L, Zhang S, Zheng L, Wu H J, Wang B K, He Z Y, Jin Z W, Ye C C and Wang G 2023 *IEEE Trans. Electron Devices* **70** 5497

Online First Press

[73] He Z Y, Zhang G L, Zhang S, Feng X Q, Liu Z D, Wang G, Yang S W and Ding G Q 2021 *Appl. Phys. Lett.* **119** 232104
[74] Courtin J, Tricot S, Delhaye G, Turban P, Lépine B, Le Breton J C and Schieffer P 2020 *Phys. Rev. B* **102** 245301
[75] Zhu W, Feng X Q, Liu Z D, Zhao M H, He P, Yang S W, Tang S W, Chen D, Guo Q L, Wang G and Ding G Q 2021 *ACS Appl. Mater. Interfaces* **13** 23081
[76] He Z Y, Zhang S, Zheng L, Liu Z Y, Zhang G L, Wu H J, Wang B K, Liu Z D, Jin Z W and Wang G 2022 *IEEE Electron Device Lett.* **43** 1818
[77] He Z Y, Yu L Y, Wang G, Ye C C, Feng X Q, Zheng L, Yang S W, Zhang G L, Wei G W, Liu Z D, Xue Z Y and Ding G Q 2022 *ACS Appl. Mater. Interfaces* **14** 14764
[78] Yang J, Tang L L, Luo W, Shen J, Zhou D H, Feng S L, Wei X Z and Shi H F 2019 *ACS Appl. Mater. Interfaces* **11** 30421
[79] Teshima T F, Henderson C S, Takamura M, Ogawa Y, Wang S, Kashimura Y, Sasaki S, Goto T, Nakashima H and Ueno Y 2019 *Nano Lett.* **19** 461
[80] Xiao S Y, Wang T, Liu Y B, Xu C, Han X and Yan X C 2016 *Phys. Chem. Chem. Phys.* **18** 26661
[81] Hu B, Kong L B, Kang L, Yan K, Zhang T, Li K and Luo Y C 2017 *RSC Adv.* **7** 14516
[82] Wang B K, Li Z, Wu H J, Zhang S, Zhang G L, Zhang J Q, Lian S S, Zheng L, Xue Z Y, Yang S W, Ding G Q, Xu W W, Tang S W and Wang G 2024 *Small Struct.* **5** 2300418
[83] Lian S S, Zhang J Q, Zhu F H, Cao G Q, Ma H, Xu Z H, Xu W W, Zheng L, Dai J Y and Wang G 2025 *Chem. Eng. J.* **522** 167291
[84] Zhang S, Zhang G L, Ding G Q, Liu Z D, Wang B K, Wu H J, Wei G W, Li J, Ye C C, Yang S W and Wang G 2024 *ACS Nano* **18** 4944
[85] Thiyagarajan P 2021 *IET Nanobiotechnol.* **15** 348
[86] Yang J, Yang Q, Zhang Y N, Wei X Z and Shi H F 2023 *RSC Adv.* **13** 22838
[87] Li H, Shi Y C, Shang H, Wang W M, Lu J, Zakharov A A, Hultman L, Uhrberg R I G, Syvajarvi M, Yakimova R, Zhang L Z and Sun J W 2020 *ACS Nano* **14** 4905
[88] Bai Z Q, Xiao Y, Luo Q, Li M M, Peng G, Zhu Z H, Luo F, Zhu M J, Qin S Q and Novoselov K 2022 *ACS Nano* **16** 7880
[89] Lu Y H, Feng S R, Wu Z Q, Gao Y X, Yang J L, Zhang Y J, Hao Z Z, Li J F, Li E P, Chen H S and Lin S S 2018 *Nano Energy* **47** 140
[90] Lian S S, Cao G Q, Ma H, Li S B, Qian K, Zhang J Q, Zheng L and Wang G 2026 *IEEE Trans. Electron Devices* **73** 3696
[91] Chang C C, Chi C Y, Yao M, Huang N, Chen C C, Theiss J, Bushmaker A W, LaLumondiere S, Yeh T W, Povinelli M L, Zhou C, Dapkus P D and Cronin S B 2012 *Nano Lett.* **12** 4484
[92] Wu H J, Zhang J Q, Lian S S, Wang B K, Zheng L, Ye C C and Wang G 2024 *IEEE Electron Device Lett.* **45** 1245
[93] Wang P, Li X Q, Xu Z J, Wu Z Q, Zhang S J, Xu W L, Zhong H K, Chen H S, Li E P, Luo J K, Yu Q K and Lin S S 2015 *Nano Energy* **13** 509
[94] Liang F X, Wang J Z, Li Z P and Luo L B 2017 *Adv. Opt. Mater.* **5** 1700081
[95] Wu Y, Yan X, Zhang X and Ren X M 2016 *Appl. Phys. Lett.* **109** 183101
[96] Wu W, He W, Ling D D, Chen L, Zhang Y Z, Fan X Q, Bi Y H, Wang D B and Wang J Z 2025 *Small* **21** 2501484
[97] Mukherjee S, Dan S, Bera A and Pal A J 2026 *Nano Lett.* **26** 4234
[98] Balasubramani V, Chandrasekaran J, Manikandan V, Le T K, Marnadu R and Vivek P 2021 *Surf. Interfaces* **25** 101297
[99] Godavarthi S, Kushvaha S S, Saha D, Altaf M, Nallabala N K R, Yuvaraj C, Reddy M R, Kesarla M K, Bakash K R, Krishna G G, Rosaiah P, Karthik T V K and Minnam Reddy V R 2024 *Ceram. Int.* **50** 31845
[100] Wu H J, Lian S S, Zhang J Q, Wang B K, Bai W J, Ding G Q, Yang S W, Liu Z D, Zheng L, Ye C C and Wang G 2025 *Small* **21** 2406164
[101] Lian S S, Liu Z Y, Fu X L, Zhu F H, Zhang J Q, Cao G Q, Ma H, Tang S W, Zheng L, Xu W W and Wang G 2025 *Nano Lett.* **25** 6583
[102] Zhang J Q, Chen L F, Zhu F H, Lian S S, Cao G Q, Ma H, Wang H, He P, Ding G Q, Wang G, Ye C C and Yang S W 2026 *Adv. Funct. Mater.* **36** e18271
[103] Poddar K, Sinha R, Jana B, Chatterjee S, Mukherjee R, Maity A R, Kumar S and Maji P S 2023 *Appl. Opt.* **62** 8190
[104] Zhan Y, Cheng Q, Song Y and Li M 2022 *Adv. Funct. Mater.* **32** 2200385
[105] Ghosh S, Mukhopadhyay B and Chang G E 2020 *IEEE Sens. J.* **20** 7801
[106] Devi N M, Baqais A A, Debnath A K, Alam M W and Singh N K 2022 *Ceram. Int.* **48** 30107
[107] Li Q, Huang J, Meng J and Li Z 2022 *Adv. Opt. Mater.* **10** 2102468
[108] Wang B K, Zhang J Q, Lian S S, Wu H J, Liu Z D and Wang G 2024 *Appl. Phys. Lett.* **125** 142103
[109] Zhang J Q, Ma H, Cao G Q, Lian S S, Xue Z Y, Dai J Y and Wang G 2025 *IEEE Electron Device Lett.* **46** 2241
[110] Sharma T, Kwon H, Park J, Han S, Son G, Jung Y and Yu K 2018 *Opt. Commun.* **427** 452
[111] Learkthanakhachon S, Taghizadeh A, Park G C, Yvind K and Chung I S 2016 *Opt. Express* **24** 16512
[112] Ibrahim M, Aouassa M, Torrisi L, Cutroneo M, Aladim A K, Saron K M A, Ghalab S, Mohamed Z and Berbezier I 2026 *Vacuum* **248** 115196
[113] Li J H, Liu Q, Ho D, Zhao S F, Wu S W, Ling L, Han F, Wu X, Zhang G, Sun R and Wong C P 2018 *ACS Appl. Mater. Interfaces* **10** 9727
[114] Wang X P, Hu A P, Chen X H, Liu J L, Li Y H, Li C Y, Wang H and Tang Q L 2022 *J. Cent. South Univ.* **29** 1761
[115] Wu C, Fang L J, Huang X Y and Jiang P K 2014 *ACS Appl. Mater. Interfaces* **6** 21026
[116] Yuan Z, Ding P, Niu L Y, Wang Z H, Jia X and Xu J H 2025 *ACS Appl. Electron. Mater.* **7** 1502
[117] Zhang J Q, Lian S S, Zhu F H, Cao G Q, Ma H, Wang B K, Wu H J, Zhao Z, Liu Z D and Wang G 2025 *J. Mater. Chem. C* **13** 3414
[118] Li J H, Xia B L, Xiao X, Huang Z F, Yin J, Jiang Y, Wang S, Gao H, Shi Q W, Xie Y N and Chen J 2023 *ACS Nano* **17** 19232
[119] Yilmaz O F and Kirca M 2025 *Comput. Mater. Sci.* **247** 113544
[120] Jing L, Cheng R, Garg R, Gong W, Lee I, Schmit A, Cohen-Karni T, Zhang X and Shen S 2023 *ACS Nano* **17** 2602
[121] Movaghgharnezhad S, Kim M, Lee S M, Jeong H, Kim H, Kim B G and Kang P 2023 *Mater. Des.* **231** 112019
[122] Han J Y, Fu Z Y, Wei J X, Han S, Deng W J, Hu F C, Wang Z, Zhou H X, Yu H, Gou J and Wang J 2025 *Light Sci. Appl.* **14** 362
[123] Ahn J, Yeon E and Hwang D K 2025 *Adv. Opt. Mater.* **13** 2403412
[124] Zhang Z, Ji P R, Hu W B, Qin S H, Zhao S H, Dong H J, Tao W H and Yang S M 2025 *Microsyst. Nanoeng.* **11** 243
[125] Ma H, Yin A L, Cao G Q, Li S B, Qian K, Zhang J Q, Lian S S, Xu W W, Xue Z Y, Zheng L, Guo Q L and Wang G 2026 *Nano Lett.* **26** 5556
[126] Chen Y F, Wang Y, Wang Z, *et al*. 2021 *Nat. Electron.* **4** 357
[127] Chen Z C, Ji F, Li Y D, Wang Y H, Ge X H, Jiang K, Zhu H and Wang X H 2025 *Chin. Phys. B* **34** 128501
[128] Wu P S, Ye L, Tong L, Wang P, Wang Y, Wang H L, Ge H N, Wang Z, Gu Y, Zhang K, Yu Y Y, Peng M, Wang F, Huang M, Zhou P and Hu W D 2022 *Light Sci. Appl.* **11** 6
[129] He T, Ma H, Wang Z, Li Q, Liu S N, Duan S K, Xu T F, Wang J C, Wu H T, Zhong F, Ye Y T, Wu J H, Lin S, Zhang K, Martyniuk P, Rogalski A, Wang P, Li L, Lin H T and Hu W D 2024 *Nat. Photon.* **18** 60

CPB Online First Press